Temperature induced change in aliphatic monolayers observed by vibrational sum-frequency generation spectroscopy

Dissertation
zur Erlangung des akademischen Grades eines
Doktors der Naturwissenschaften
– Dr. rer. nat. –

vorgelegt von

Jan Weber

geboren in Duisburg

Fakultät für Chemie
der
Universität Duisburg-Essen

2014

Die vorliegende Arbeit wurde im Zeitraum von September 2010 bis August 2014 im Arbeitskreis von **Prof. Dr. Eckart Hasselbrink** unter Anleitung von **Dr. Thorsten Balgar** in der Fakultät für Chemie der Universität Duisburg-Essen durchgeführt.

Tag der Disputation: 23.10.2014

Gutachter:	Prof. Dr. Eckart Hasselbrink
	Prof. Dr. Sebastian Schlücker
Vorsitzender:	Prof. Dr. Matthias Epple

Contents

Abstract

In the context of the presented thesis organic monolayers have been studied. In this context essential two different sample systems have been analyzed at temperatures between 300 and 500 K. The analytical method used for the characterization is the so-call sum-frequency generation spectroscopy, an inherently surface specific form of vibrational spectroscopy. By monitoring various vibrational modes with respect to temperature change conclusions regarding the microscopical structure within the monolayer can be drawn. In this context it was also possible to draw conclusions with respect to the reaction enthalpy for conformational changes.

Zusammenfassung

Im Rahmen der vorliegenden Dissertation wurden organische Monoschichten untersucht. Dabei wurden im Wesentlichen zwei verschiedene Probensysteme im Temperaturbereich von 300 bis 500 K untersucht. Bei der zur Charakterisierung verwendeten Analysemethode handelt es sich um die sogenannte Summenfrequenz Spektroskopie, eine inhärent oberflächenspezifische Schwingungsspektroskopie. Durch die Beobachtung verschiedener Schwingungsmoden im Temperaturverlauf lassen sich Rückschlüsse über mikroskopische Struktur innerhalb der Monoschicht ziehen. Es war in diesem Zusammenhang auch möglich, Rückschlüsse auf Reaktionsenthalpien für Konformationsänderungen zu ziehen.

1. Introduction

In our everyday life we are surrounded by surfaces of all kinds. As surfaces often define the properties of materials or applications, they are of prime interest to science and industry. This is especially true since some surface properties are fundamentally different to the ones of the respective bulk material.

Organic monolayers are of great interest in this context, as there are diverse possibilities to attach them to a given surface, as well as tune their properties by modification of specific molecular moieties. Some polymers, such as poly(N-isopropylacrylamide) (PNiPAAm), are even switchable by an external stimulus with regard to certain characteristics [1].

As is to be expected scientific interest on this subject dates back quite some time. One early example of surface science is the work of *Agnes Pockels*, who made one of the first studies on organic monolayers on water, that was published in the year 1891 with the help of *Lord Rayleigh* [2]. Based on this work, in later years, *Irving Langmuir* and *Katharine Blodgett* were able to develop their technique to deposit the surface of a liquid onto a solid by immersing [3, 4, 5, 6]. A method still used to this day.

Since then several other technical applications depend on surface properties. Surface properties influence tribology or corrosion [7] as well as wettability, biocompatibility and electronic characteristics. As a result it is valuable to be able to tune specific properties for certain technical applications.

It is understandable, that for some applications the molecular orientation and general order within such a monolayer may be of importance. The engineering of cell shape and function [8], the fabrication of circuits in microelectronics [9, 10] or the formation of channels in microfluidic devices [11] rely on very defined structures to ensure proper functionality.

Hence, a general and basic understanding of the structure in organic monolayers has points of contact with a diverse number of applications. In this context the experiments presented in this thesis should be seen. The sample systems examined here have been chosen to represent two candidates from a typical organic monolayer preparation. As an abundance of technical applications require elevated temperatures, experiments done here are focused around the changes within monolayers with temperature.

While there are several studies on monolayers, many methods used for the analysis lack the capability to clarify ordering phenomena on a molecular level. This is especially true, when considering realistic environmental conditions. Most technical applications will have to face room temperature and higher under ambient conditions as opposed to ultra-high vacuum and constant cooling, applied for many analytical approaches.

Therefore, vibrational sum-frequency generation spectroscopy is the method of choice used in the context of this thesis. Due to its intrinsic surface sensitivity and noninvasive character it represents an appropriate tool for the study of the described interests.

2. Principles

2.1. Organic Monolayers

While there is a multitude of organic monolayers, with an even greater variety of functions impacting diverse areas of science and application, the focus of this work is not to explain one specific phenomenon. The approach here is rather to find connecting and general characteristics in basic examples of organic monolayers and their behavior particularly with regard to changes in temperature.

For this purpose two sample systems have been carefully chosen to represent two major forms of connection between the organic molecule and the substrate, while elsewise being adequately similar and simple in composition to allow for comparison.

To this end **octadecyltrichlorosilane** is used as an example for a covalent bond substance and **eicosanoic acid** represents coating in the from of a *Langmuir-Blodgett* film. Both molecules are of amphiphilic nature, with a head group that connects to the substrate, a long aliphatic chain and a terminal methyl group. In the absence of other functionalities both molecules presumably form ordered monolayers with all-*trans* configurated chains.

2.1.1. Octadecyltrichlorosilane

Octadecyltrichlorosilane (OTS) is a prominent example for a covalently bound molecule, due to its characteristic to form *self-assembled monolayers* (SAM).

The commonly assumed mechanism of the silanation reaction starts with OTS as a precursor and can basically be broken down into three steps. OTS is hydrolyzed, adsorpt at the substrate and finally condensed by water elimination, leading to a chemically anchored monolayer [12]. See Fig. 2.1.

During adsorption the molecule's contact to the substrate is dominated by hydrogen bonds that allow for a rather high mobility [14]. This mobility is restricted once condensation starts and OTS molecules are being bound to neighboring molecules and the substrate by covalent bonds [15].

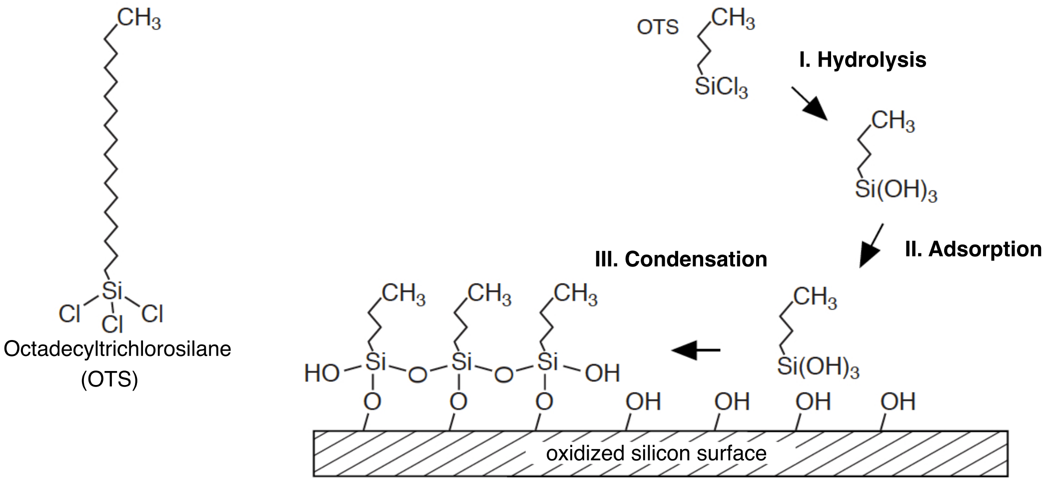

Figure 2.1.: Schematic representation of the silanation reaction[13, 12]

Following this general mechanism a two-dimensional network is grafted. However, different reaction courses have been described, essentially discerning between an "uniform" and an "island-type" growth model [16].

In the uniform growth model solitary OTS molecules are orderless distributed at the surface and gradually a monolayer is formed. Molecules in this model are believed to be strongly tilted, resulting in a low monolayer hight at low surface coverage. With increasing coverage the layer is continuously denser packed and molecules change their tilt angle by standing more erect. The resulting change in monolayer hight may be seen as an indicator for this growth model [16].

The island-type growth model assumes a pre-polymerization of OTS molecules in the solution that are then bound to the surface. The growth then proceeds by adding single molecules at the edge of the island as well as joining larger agglomerates. In this growth mechanism molecules are believed to stand upright, resulting in no change of monolayer hight during the formation [16]. This growth type has also been simulated by considering the adsorption, diffusion, grafting, and cross-linking of silanol clusters [17].

While both growth types are capable of forming a closed monolayer, the predominance of one or the other model is tightly linked to the experimental conditions used. In particular, the water content and temperature of the OTS solution are of importance. In this regard, a higher water content facilitates pre-polymerization and therefore larger islands, while dryer conditions typically lead to a more uniform reaction type [18].

Similarly, *Carraro et al.* find that solution temperatures of 10 °C or lower favor island growth, while temperatures above 40 °C promote uniform growth [14]. Yet, temperature and the water content in the precursor solution cannot be seen in an isolated manner [19].

A mixture of both growth mechanisms can be expected under the experimental conditions used here (see chapter 3.3) [13]. The resulting monolayer can be characterized as a densely packed film, with molecules in a mainly undistorted hexagonal local order [20] and a mean molecular area of 20.2 $Å^2$ [20, 7]. Molecules may be tilted to angles between 7° and 30° with respect to the surface normal [21].

Even though imperfections such as *pinholes* [22] and *gauche* defects [23] have been reported, OTS monolayers generally are considered to be mechanically [24, 25], chemically [26] and thermal [27, 28] stable [13].

2.1.2. Eicosanoic acid

Eicosanoic acid, also called arachidic acid, is the other major sample system this thesis is based on. Like OTS it is an amphiphilic molecule with a long aliphatic chain, in this case a 20-carbon chain with the acid moiety at the end.

In contrast to OTS, arachidic acid does not arrange itself to a complete monolayer in a self-assembly process. Instead, a monolayer is formed by applying external pressure, utilizing a Langmuir trough. In this process arachidic acid molecules are initially loosely distributed on a water surface and then compressed to a closed monolayer, before being transferred to the substrate of choice (see below for details).

To increase packing density as well as stability of the so formed layer divalent counterions such as Cd^{2+} or Ca^{2+} may be introduced to the water subphase[1] [29]. These counterions are able to bridge arachidic acid molecules. Bridging is especially effective for fatty acid molecules in the dissociated state, which is why an alkaline pH value in the subphase is of an advantage [30].

Monolayers of the $[CH_3(CH_2)_{18}COO^-]_2M$ ($M = Cd^{2+}$, Ca^{2+}) type are arranged in a hexagonal lattice with a mean molecular area of 19.7 $Å^2$ [31]. The transfer pressure also has an influence on the molecular area. While showing mostly the same properties Ca and Cd stabilized films differ in the tilt angle of the chains with respect to the surface normal. Tilt angles of 0° and 33° for Cd and Ca films, respectively, have been reported [32, 33, 34].

---

[1] The subphase is a liquid phase used in a Langmuir trough to form a monolayer on.

While imperfections such as *pinholes* [33] cannot always be excluded, a film deposition to a substrate with near perfect quality can be achieved [31, 35].

As Cd arachidate and Ca arachidate are comparable systems, Ca arachidate (CaA) has been used in the context of this thesis due to its lower toxicity.

2.2. Vibrational Spectroscopy

Spectroscopy is the study of the interaction between matter and electromagnetic radiation [36]. In the case of vibrational spectroscopy this interaction is linked to molecular vibration.

A molecule has, depending on its geometry, different possibilities to vibrate. Each is called a vibrational mode. For molecules with N atoms, linear molecules have $3N-5$ normal modes of vibration, whereas nonlinear molecules have $3N-6$ normal modes of vibration. In each normal mode of vibration all the atoms in a molecule are displaced with the same frequency and all atoms pass through their equilibrium positions simultaneously [37].

The fundamental frequencies of the normal vibrations depend on the masses of the atoms, their geometrical arrangement, the stiffness of the chemical bonds, and their molecular environment [38].

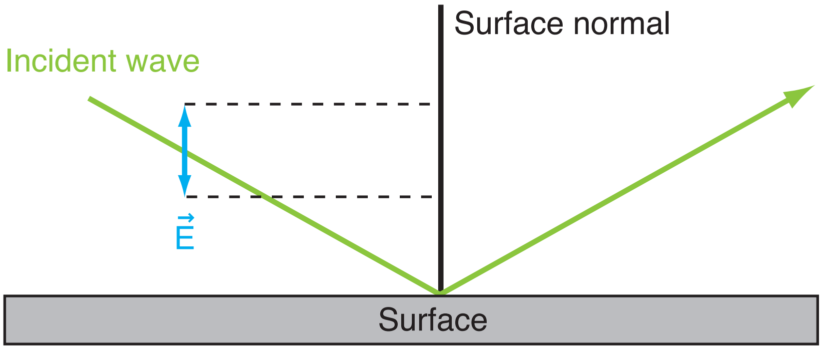

Figure 2.2.: Polarization of light

The direction of polarization of an electromagnetic wave also has an influence on the interaction with matter. The nomenclature in defining different polarizations is linked to a surface and the plane of incidence. Which is the plane spanned by the propagation vector *(Poynting vector)* of the incident wave and the surface normal.

In the case of linear polarized light a wave is called p-polarized, if the electric field vector lies in the plane of incidence. If electric field vector and plane of incidence are perpendicular to each other, the wave is called s-polarized (see Fig. 2.2).

Polarization directions in an experiment comprised of more then one electromagnetic wave are denoted in the same way. Each wave's polarization is listed separately in order of increasing wavelength. For a three wave experiment, such as SFG (see next chapter), a polarization combination of ssp would mean s-polarized sum-frequency light, s-polarized visible light and p-polarized IR light.

2.3. Vibrational Sum-Frequency Generation Spectroscopy

Vibrational *sum-frequency generation* (SFG) spectroscopy is an optical non-linear method akin to *second harmonic generation* (SHG) and was first introduced 1987 by *Y. R. Shen* and coworkers [39].

The name SFG directly relates to the method's principle, where two laser beams are overlapped at a surface generating a new beam at the sum of the frequencies of the incident beams.

The method is intrinsically surface sensitive making it a powerful, unique tool for the study of surfaces and interfaces, as will become apparent in the following sections.

2.3.1. Principles

The result of the interaction of a weak electric field $\vec{E}$ from a light source with matter may be described as a polarization $\vec{P}$ within a linear approximation:

$$\vec{P} = \epsilon_0 \chi \vec{E} \tag{2.1}$$

Where ϵ_0 is the vacuum dielectric constant [2] and χ the susceptibility. The polarization is a measure for charge distribution or a displacement of the electron cloud. An induced dipole may result, in turn able to emit an electromagnetic wave.

This model, however, only holds true until the external electric field becomes comparable in strength to the intramolecular field felt by an electron. The linear polarization of matter is no longer a sufficient approximation and higher order terms have to be taken into account. The total polarization, using the electric dipole approximation, is then expanded into a series expansion [41]:

$$\vec{P} = \epsilon_0 \left(\chi^{(1)} \vec{E} + \chi^{(2)} \vec{E}^2 + \chi^{(3)} \vec{E}^3 + ... \right) \tag{2.2}$$

$\chi^{(n)}$ are the linear and non-linear susceptibilities of the n^{th} order and are tensorial quantities. For two light waves of the frequencies ω_1 and ω_2 and the amplitudes $E_{0,1}$ and $E_{0,2}$ the first non-linear term gives rise to mixing:

$$\vec{P}^{(2)} = \epsilon_0 \chi^{(2)} \left(\vec{E}_{0,1}\ cos(\omega_1 t) + \vec{E}_{0,2}\ cos(\omega_2 t) \right)^2 \tag{2.3}$$

---

[2] $\epsilon_0 = 8.854 \cdot 10^{-12} \frac{As}{Vm}$ [40]

Eq. 2.3 may then be solved to:

$$\begin{aligned}\vec{P}^{(2)} = \epsilon_0\chi^{(2)}\Big(&\frac{1}{2}\vec{E}_{0,1}^2 + \frac{1}{2}\vec{E}_{0,2}^2 \\ &+ \frac{1}{2}\vec{E}_{0,1}^2\ cos(2\omega_1 t) + \frac{1}{2}\vec{E}_{0,2}^2\ cos(2\omega_2 t) \qquad \textbf{(SHG)} \\ &+ \vec{E}_{0,1}\vec{E}_{0,2}\ cos(\omega_1+\omega_2)\ t \qquad \textbf{(SFG)} \\ &+ \vec{E}_{0,1}\vec{E}_{0,2}\ cos(\omega_1-\omega_2)\ t\ \Big) \qquad \textbf{(DFG)}\end{aligned} \tag{2.4}$$

The shown polarization components (eq. 2.4) are generated with the sum (SFG) and the difference (DFG) frequencies of two incident waves. In the case of $\omega_1 = \omega_2$ second harmonic generation (SHG) occurs. Principles regarding SFG equally hold true to DFG, but are not important in the context of this thesis and will therefore be ignored in further discussions.

When considering the SFG intensity of a densely packed monolayer *Vidal* and *Tadjeddine* [42] find

$$I \propto \frac{\beta^2}{[1+\alpha_\nu\tilde{U}]^2[1+\alpha_e\tilde{U}]^4} \tag{2.5}$$

where β is the hyperpolarizability[3] of the adsorbed molecules, α_ν and α_e are the vibrational and electronic polarizabilities respectively, and $\tilde{U}$ is the so-called dipole sum that depends on the two-dimensional arrangement of the molecules in the plane of the substrate [43, 44, 45, 46, 47]. In the case of an incomplete layer, the signal is [42, 48]

$$I \propto \frac{\Theta^2\cdot\beta^2}{[1+\alpha_\nu\Theta\tilde{U}]^2[1+\alpha_e\Theta\tilde{U}]^4} \tag{2.6}$$

where Θ is the fractional coverage ($\Theta = 1$ corresponds to a saturated monolayer) of the molecules.

Considering eq. 2.5 and 2.6 it becomes apparent that it is necessary to relate the nonlinear properties of the molecule, described by the hyperpolarizability β, with the experimentally accessible, macroscopic susceptibility $\chi^{(2)}$. This involves the transformation of β from the molecular coordinate system (*abc*) to the surface coordinate system (*xyz*): $\beta_{abc} \Rightarrow \beta_{xyz}$ [41].

---

[3] The hyperpolarizability is a nonlinear-optical property of a molecule. It describes the second-order electric susceptibility per unit volume.

Under the assumption of averaging over many molecules, an orientational distribution and no interaction between the molecular fragments, the susceptibility $\chi^{(2)}$ may be seen as the macroscopic hyperpolarizability β, such that

$$\chi^{(2)} = N\langle\beta\rangle \tag{2.7}$$

with N as the number of SFG active molecules and the angle brackets indicating averaging over all possible molecular orientations.

According to *Buck* and *Himmelhaus* [41] the hyperpolarizability β is defined as follows:

$$\beta_{\nu,xyz} = \frac{\alpha_{\nu,xy}\ \mu_{\nu,z}}{\omega_{IR} - \omega_{\nu} + i\Gamma_{\nu}} \tag{2.8}$$

Here ω_ν and Γ_ν are the resonance frequency of the mode ν and its bandwidth, while $\alpha_{\nu,xy}$ and $\mu_{\nu,z}$ are the Raman and IR transition dipole moments respectively [41, 49].

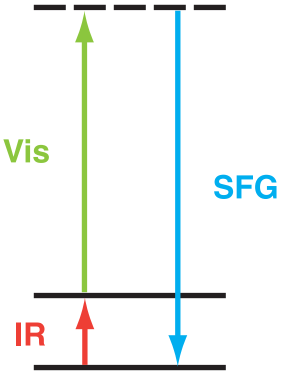

Figure 2.3.: Schematic illustration of the SFG process. Energy levels shown represent the vibrational ground state, the first excited state (solid lines) and a virtual state (dashed line).

Equation 2.8 emphasizes a very important selection rule for SFG spectroscopy: *a vibrational mode must be IR* ***and*** *Raman active to be SFG active.* If either $\alpha = 0$ or $\mu = 0$, β and ultimately $\chi^{(2)}$ would be zero, resulting in no SFG contribution.

This principle is also schematically illustrated in Fig. 2.3. The SFG generation is shown as a combination of IR excitation from the vibrational ground state to the first excited state with a simultaneous Raman de-excitation, using visible light, via a virtual state relapsing into the ground state resulting in the generation of one new SFG photon. Hence, IR and Raman activity is needed.

2.3.2. Spectral Analysis

On closer inspection of the principles of sum-frequency generation the advantages and problems of this method for spectroscopy become understandable.

While recording an SFG spectrum two laser beams will typically be employed in order to achieve electric field strengths necessary for non-linear polarization. Generally two categories of SFG arrangements can be distinguished:

1. A picosecond laser system with narrow-band IR light that may be tuned to a range of frequencies during an experiment.
   A system of this kind was used for the experiments conducted in this thesis.

2. A femtosecond laser system utilizing broad-band IR light of a constant center frequency. In this case the generated SF light is spectrally resolved after generation.
   Other groups have successfully employed this technique e.g. [50].

In both cases the beams are overlapped on the sample surface, spatially and temporally.

The resulting spectrum is therefore a plot of SFG intensity versus IR frequency. Peaks appear, when a resonance is met, often resulting in a *Lorentzian* like shape. For this reason SFG spectra can often be fitted to a function of Lorentzian type:

$$y = y_0 + \frac{A}{(x - x_0)^2 \ + \ B} \tag{2.9}$$

For a more accurate description of measured data it is however feasible to use an equation like eq. 2.8, including a dampening constant of complex form.

As mentioned earlier SFG spectroscopy is of great import to surface science, due to its intrinsic symmetry sensitivity.

This characteristic is directly linked to the selection rule referred to before. In order to be SFG active a normal mode must be IR and Raman active. Yet, symmetry considerations lead to the so-called *rule of mutual exclusion*, which states that no fundamental mode of a molecule with a center of symmetry can be both infrared and Raman active at the same time [51, 52].

As a result any centrosymmetric environment cannot contribute to an SFG signal. Since all fluid media are centrosymmetric according to statistical distribution as well as many solids due to their lattice structure, their matrix effects can effectively be stalled from SFG measurements. As a contributor always remains any interface, where centrosymmetry must be broken locally.

It is noteworthy that in the case of SFG such a signal is created through the generation of new photons. As their wavelengths are in the visible spectral region, a single photon detection via photomultiplier is possible. This is in contrast to most linear optical methods used for interface studies such as infrared reflection absorption spectroscopy (IRRAS), ellipsometry or methods which relay on evanescent fields.

Even in the case of a non-centrosymmetric substrate or bulk phase, SFG spectroscopy can be applied. In this case the source term of the sum-frequency signal $P(\omega)$ can be separated into an interface contribution P^I and a bulk term P^B as pointed out in detail by *Y. R. Shen* [41, 53]:

$$P(\omega) = P^I(\omega) + P^B(\omega) \tag{2.10}$$

As the bulk part mainly is a non-resonant contribution[4] in the observed spectral region, the sum-frequency signal is notably enhanced once a resonant interface contribution comes into appearance.

Taking a non-resonant background into account a fit function to describe the total SFG intensity can be found based on eq. 2.8 [42]:

$$I \propto \left| \left| \chi^{(2)}_{NR} \right| e^{i\xi} + \sum_{\nu} \frac{A_\nu}{\omega_{IR} - \omega_\nu - i\Gamma_\nu} \right|^2 \tag{2.11}$$

$\chi^{(2)}_{NR}$ here is the non-vibrationally resonant part of the signal, which can be related to the resonant part using ξ as the relative phase between the resonant and non-resonant signals. A_ν is the combined IR and Raman transition moment of the mode ν.

While SFG spectroscopy is a powerful surface science tool, some caution is advised, when working with this method:

- Only assemblies of molecules with a net orientation will give rise to an SFG signal, since the average hyperpolarizability will otherwise be zero ($\langle\beta\rangle$ in eq. 2.7).
- The use of different polarization combinations may lead to the presence or absence of individual lines in a spectrum of the same sample, due to symmetry

---

[4] In the observed spectral region the bulk contribution is independent of the IR wavelength.

or orientational considerations.

2.3.3. Orientation Analysis

As the presence of individual lines in an SFG spectrum depends on the polarization combinations used, it is possible to utilize this as method to gain insight into orientational parameters of SFG active groups.

Therefore it is advisable to remember, that β as well as $\chi^{(2)}$ are third rank tensors and accordingly are comprised of 27 elements (3x3x3). Next it is necessary to identify the independent and non-vanishing components of that tensor. This is done by consideration of molecular symmetry with the help of character tables. The majority of these elements, for example, vanish, because $\chi^{(2)}$ has to be invariant under any symmetry operation S that preserves the interface or the substrate structure.

In the case of an isotropic surface, this leads to a reduction to seven non-vanishing elements [42].

Additionally, the transformation from the molecular to the laboratory coordinate system is performed in terms of Euler angles.

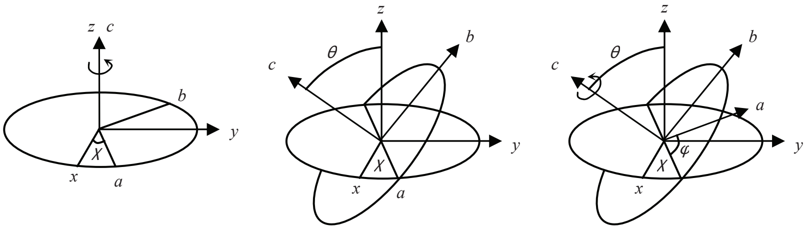

Figure 2.4.: Euler angle transformation (χ, θ, ϕ) between molecular coordinates (a, b, c) and laboratory coordinates (x, y, z).

In Fig. 2.4 χ is the azimuthal angle, θ the tilt angle and ϕ the twist angle.

Having isolated appropriate non-vanishing elements for the mode in question, it is possible to derive the tilt angle of a (rod-like) molecule on a surface by comparing SFG signal intensities obtained using different polarization combinations.

Results from this kind of calculation should be taken with a grain of salt, however, as it should be noted that the value of the angle determined using this method depends sensitively on the optical constants used to calculate the Fresnel factors, particularly the value for the interfacial dipolar sheet that is unknown in general [42, 54]. Fresnel factors describe the behavior of electromagnetic waves at the interface between media with differing refraction indices, in particular the magnitude of the local electric fields of the three interacting optical beams at the interface. The local electric field strengths depend not only on the intensity of the incident beams but also on the bulk, linear refractive indices of the different layers of the sample [55].

2.4. Langmuir-Blodgett Films

A so-called *Langmuir-Blodgett film* (LB surface) consists of one or more monolayers of an organic material, deposited onto a solid from the surface of a liquid.

First experiments in the area of monomolecular layers are based on the work of *Agnes Pockels* and have been published in *Nature*,1891 [2]. Based on these findings *Irving Langmuir* in collaboration with *Katharine Blodgett* succeeded to establish a scientific explanation for Pockels' work and prepare so-called "Langmuir-Blodgett films" in the laboratory.

2.4.1. Film Preparation

Today the typical setup to prepare an organic LB film consists of a so-called *Langmuir trough* and a film balance to monitor the change in density of the molecules used for the film.

A Langmuir trough today is a fully computerized cavity, typically made of Teflon, with one or more movable barriers that allow control of the pressure applied on the monolayer [56]. The trough's cavity is filled with a so-called subphase. The most commonly used subphase is water, although mercury and other materials as well as glycerol have been used [56].

Atop this subphase a solution of molecules that will form the monolayer is spread. These molecules must be of amphiphilic[5] nature in order to arrange themselves at the gas/subphase interface.

Using the movable barriers one may now reduce the surface area, compressing the spread amphiphiles in the process. The film balance monitors the change in surface pressure (π) while this happens. Usually the resulting phase development is characterized by a π/A-diagram, where A is the surface area, often expressed as an area per molecule.

As experiments of this kind are performed at variable, yet fixed temperatures these π/A-diagrams may also be referred to as isotherms.

The generalized isotherm presented in Fig 2.5 exemplarily shows the different phases the molecules atop the subphase may pass and gives a schematic overview of their orientation.

While there is space in abundance, which is, in analogy to the three dimensional system, called *gaseous* phase (g). The film pressure is, however, usually so small

---

[5] Amphiphile describes a chemical compound possessing both hydrophilic and lipophilic properties.

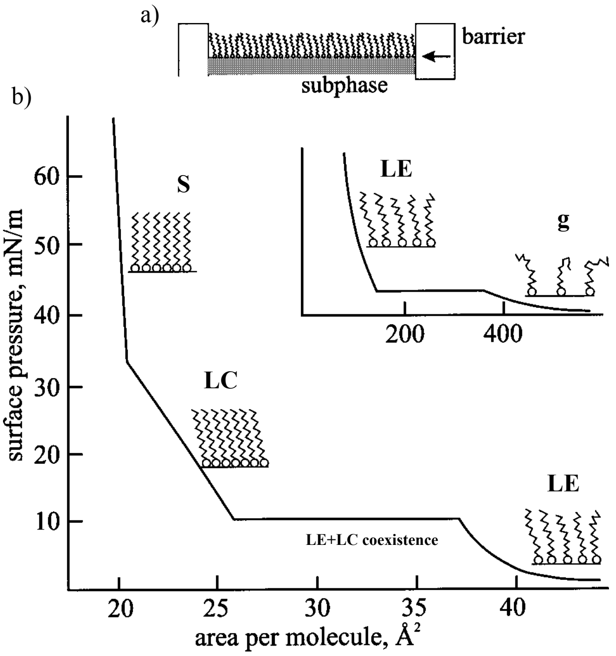

Figure 2.5.: a) A schematic diagram of a Langmuir trough. b) A generalized isotherm of a Langmuir monolayer. In the style of [57]

that it is almost undetectable. The average area per molecule on the surface is much larger than the size of the molecule [58]. There is virtually no interaction between the amphiphiles.

When compressing the gaseous phase, there will be a phase transition to the liquid state (L). The liquid state is characterized by a significant lateral interaction between the amphiphiles. There is a further discrimination between two forms of the liquid phase: the *liquid-expanded* (LE or L_1) and the *liquid-condensed* (LC or L_2) phase. In the case of the LE phase the polar heads are touching each other, while there is no lateral order in the long-chain hydrocarbons. After the LC phase is reached the amphiphiles exhibit a tilted phase with a decreasing tilt angle (measured against the normal to the subphase). The film is relatively stiff, but there is still some water present between the headgroups [58].

Finally due to even further compression the *solid* phase (S) is reached. Here the head groups are largely dehydrated and the tilt angle of the chains approaches 0° with respect to the surface normal. The area per molecule corresponds to the molecular cross-section, hence molecules are densely packed. Further compression results in a so-called *collapse* of the film, as three-dimensional domains are formed.

While there is no uniformity in the nomenclature of the different phases and their exact definition, in the context of this thesis nomenclature will be used in accordance to *Butt, Graf* and *Kappl* [58].

2.4.2. Surface Pressure Measurement

While there are different methods to obtain the surface pressure, in the context of this thesis the method of choice is the so-called *Wilhelmy* method.

With this method a Wilhelmy plate is immerged into the subphase and on the other end connected to a fine balance. These plates are usually on the order of a few square centimeters in area and often made from filter paper, glass or platinum.

The force (F) on the plate due to wetting is measured by the balance and used to calculate the surface tension (γ)

$$\gamma = \frac{F}{l \cdot cos\theta} \tag{2.12}$$

where l is the wetted perimeter of the Wilhelmy plate and θ is the contact angle between the liquid phase and the plate.

Under the assumption that the surface tension of the LB film (γ) is different from that of the pure water subphase (γ_0) and an idealized wetting ($\theta = 0$), the change in force is given by:

$$\Delta F = \frac{\gamma_0 - \gamma}{l} \tag{2.13}$$

With the definition for the surface pressure (π)

$$\pi = \gamma_0 - \gamma \tag{2.14}$$

it becomes apparent that the change in force measured by the balance is proportional to the surface pressure.

$$\pi \propto \Delta F \tag{2.15}$$

3. Experimental Setup and Materials

3.1. Optical Setup

3.1.1. Laser System

The heart of the optical setup, used for the SFG experiments, is the active-passive mode-locked Nd:YAG[1] laser system PL2143A/20, *Co. Ekspla*. This laser emits light of 1064 nm wavelength, with a pulse duration of about 25 ps and a repetition rate of 20 Hz.

Connected to the laser system is a harmonics unit as well as an optical parametric generator (PG501DFG, *Co. Ekspla*). The harmonics unit is capable of generating the second (532 nm) harmonic of the fundamental by utilizing a BBO[2] crystal. The second harmonic is used as the visible part for the SFG laser experiments.

Another part of the second harmonic light as well as a part of the fundamental are used to pump the optical parametric generator (OPG). The visible light thereby pumps an optical parametric oscillator (OPO) with a downstream optical parametric amplifier (OPA). As a result there is a so-called *signal-* (680 - 1064 nm) and a *idler-*wave (1064 - 2300 nm) at different exits of the OPG. Additionally the idler-wave may be used for difference frequency generation (DFG) with the fundamental beam utilizing a $AgGaS_2$[3]-crystal to generate tunable IR light in the spectral region of 2300 - 10000 nm.

---

[1] Neodymium-doped yttrium aluminum garnet (Nd:$Y_3Al_5O_{12}$), a crystal that is used as a lasing medium

[2] Beta barium borate (β-BaB_2O_4), a nonlinear optical material

[3] Silver gallium sulfide, a nonlinear optical material

3.1.2. Optical Components

Polarization and energy control

In order to change the polarization direction of the visible and IR laser beams $\lambda/2$ wave plates were used. In the case of IR light a tunable MgF_2 phase retardation plate wavelength range 2000 - 6500 nm (*Co. Alphalas GmbH*), was used.

To adjust the energy levels of the beams one may apply different pumping powers of the fundamental laser. This will result in different visible as well as IR powers. Since a maximum of IR energy at the sample is generally preferred in the cause of all experiments conducted in the context of this thesis, the OPG was usually pumped to its maximal capacity.

In contrast to that the visible beam's power should not always be at its maximum, since higher energy levels may lead to the destruction of the sample. In order to regulate the visible power a diffractive beam attenuator (*Co. TOPAG Lasertechnik GmbH*) was used. This attenuator employs optical grates of different etching depth to remove a tunable portion of the light by diffraction.

The typical pulse energies used were 70 μJ for the visible pulse and 200 μJ for the infrared pulse. The incident angles of the incoming beams are 65° (visible) and 55° (IR) with respect to the surface normal. Both pulses are slightly focused by means of an anti-reflection coated glass lens (visible) and a CaF_2 lens (IR) to have a diameter of about 1 mm on the sample surface.

Pulse synchronization

As mentioned above it is imperative to overlap both laser beams in space and time at the sample surface for an effective SFG experiment. While the spatial overlap is achieved relatively easy, since the 532 nm beam is inherently visible and the IR beam is overlapped with a red laser diode to make the adjustment more convenient, the temporal synchronization requires more effort.

In the process of temporal synchronization one utilizes the fact that the beam path of IR and visible are not of the same length, as they leave the optical setup at different exits. While the IR beam is directed to the sample surface at a direct path, the visible beam passes a so-called *delay line*.

This delay line is basically a translation stage of 7.5 cm length that can be moved by a sensitive stepper motor. Mounted on this translation stage are two mirrors at 45° angles that send an incoming beam back parallel to itself, with a small lateral displacement. The additional distance is long enough for the visible pulse to be synchronized to the arrival of the IR one.

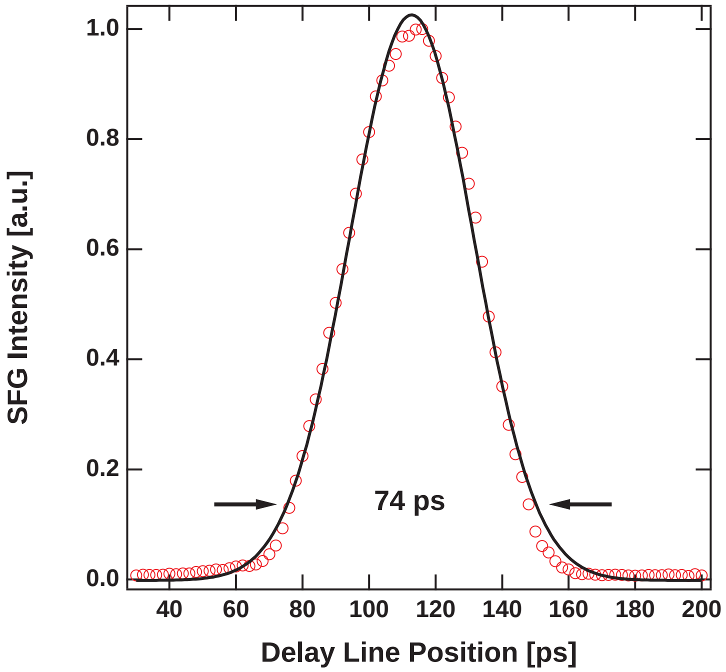

Figure 3.1.: SFG intensity from a GaAs sample as a function of delay time for the visible pulse (red markers) and a Gaussian fit (solid black line). The duration is equal to half the width at the $1/e^2$-position.

As a means of control a SFG active substance, here Gallium arsenide (GaAs), is employed. Fig. 3.1 shows the result of a typical cross-correlation using GaAs. Here one laser pulse is temporally shifted against the other and the resulting SFG intensity is recored. The delay line position is expressed as a function of time. This way it can easily be seen, how the temporal overlap of the two laser pulses results in a maximum in SFG intensity and how this intensity is lost again once the pulses are misaligned. Since the intensities of both laser pulses are described by Gaussian profiles, the combined SFG intensity also results in a Gaussian profile of doubled width. As a result the measurement of half of the peaks width at the $1/e^2$-position reveals a typical pulse duration of about 37 ps.

Sample holder

For SFG experiments conducted in the context of this thesis a custom made sample holder was used. This holder consists of a copper disc with a diameter of 4 cm and a hight of 4 mm. At the center of this disc a square cavity of 1.1 cm lateral length and a depth of 0.5 mm is used to hold the sample substrate. A clip attached to the disc may be used to clamp the sample in place as well as bring a *type K thermocouple* in contact with the sample surface for temperature measurement.

Beneath the copper disc a electric resistance heating (MICA, *Telemeter Electronic GmbH*) facilitates sample heating to about 600K.

Finally a tilt stage permits a two dimensional shift of the sample, making alignment of SFG beam and detector more comfortable.

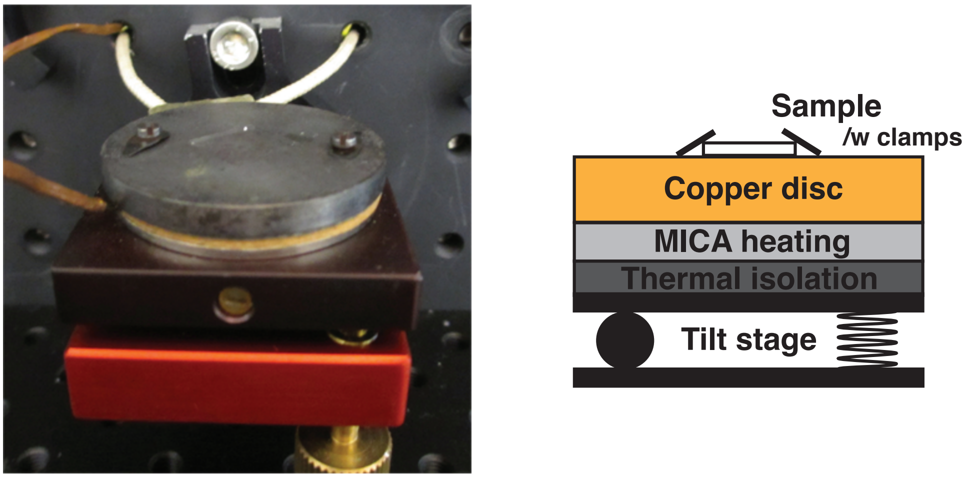

Figure 3.2.: Picture and schematic drawing of the custom made sample holder used for experiments in this thesis.

Signal separation and detection

The generated signal may only consist of a few photons, therefore a very sensitive detection method is needed. The technique of choice in such cases is a so-called *photomultiplier tube* (PMT), which utilizes the photoelectric effect to convert a photon stimulus into an electronic response.

In the context of this thesis a *Hamamatsu* R7517 PMT was used. While the wavelength of maximum response with 420 nm is close to the typical spectral region of SFG light, this detector shows a similarly strong response at longer wavelength such as the 532 nm of the incident light.

As the amount of green photons is orders of magnitudes higher than the SFG generated ones and the PMT cannot discriminate between the two, supporting components must be introduced.

The first and foremost important step is to direct the green light reflected from the sample surface away from the PMT, while ensuring a direct hit of the SFG beam. As the photons generated by sum-frequency generation are subject to conservation of momentum it is possible to calculate the angle β between the SFG and reflected, green beam following eq. 3.1 [59]

$$\beta = arcsin\left(\frac{sin\ \alpha}{(^1/\lambda_{Vis} + {}^1/\lambda_{IR})\lambda_{IR}}\right) \tag{3.1}$$

if the angle α between the incident visible and IR light as well as the respective wavelengths λ are known.

With the major part of the green light directed away from the PMT, still some effort has to be taken to discriminate the diffusely scattered residual green light. To achieve an acceptable separation a cascade of three cut-off filters (RazorEdge SP01-532RU-25, *Co. Semrock*), a notch filter (*Co. Kaiser Optical Systems*) and a long black tube to shear off scattered light are used.

Measurement and control

To measure absolute energy values for the visible and IR light a pyroelectric detector (J4-09, *Molectron*) was used. Those detectors function on the basis of piezoelectric crystals that react with a charge movement to a change in temperature. The detectors used are actively amplified. While the reaction time of the detectors is, with 1 - 2 ms, significantly slower than the PMT, it is sufficient to measure the energy from pulse to pulse.

The information retrieval of the pyroelectric detectors may be done by a device called EnergyMax 500 (*Molectron*) that directly translates the generated voltage into an energy level.

Alternatively the detectors as well as the PMT cooperate with two oscilloscopes used in the setup. An TDS 5034 (*Tektronix*) oscilloscopes handles the reading of the PMT, while a four-channel oscilloscopes Wave Runner 44Xi (*LeCroy*) is able to record other signals, such as the ones from the pyroelectric detectors.

Temporal synchronization between the different devices is realized via a digital delay- and pulse-generator (DG535, *Stanford Research Systems Inc.*).

The whole experimental control is consolidated in a personal computer system on the basis of *Microsoft Windows XP Pro SP3* with the use of *National Instruments' LabVIEW 6.1*. The LabVIEW program employed is a modified version of the one originally designed by *Dr. Kristian Laß* [59] in the first application of the laser system used for this thesis.

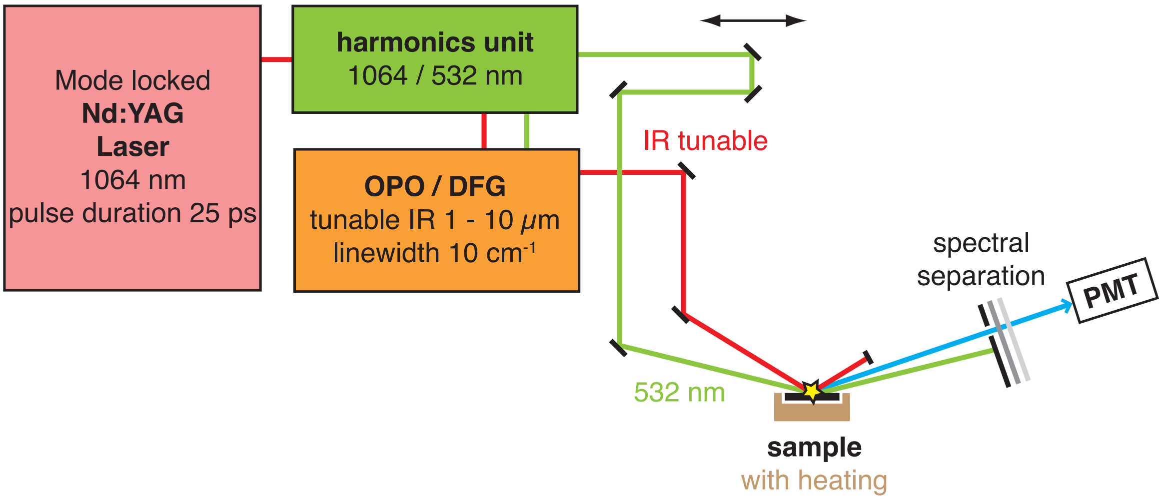

Figure 3.3.: Schematical drawing of the optical setup.

3.2. Langmuir trough

In the context of this thesis Langmuir-Blodgett films have been prepared in a Langmuir trough of the type RK 1 designed by *Riegler & Kirstein GmbH*.

The complete setup consists of the trough itself, an electronic control unit, a Wilhelmy type film balance and a dipping device, housed within a laminar flow box. The trough can be controlled by a personal computer system, also using *Microsoft Windows XP Pro SP3* in connection with a proprietary software solution compatible to *LabVIEW*.

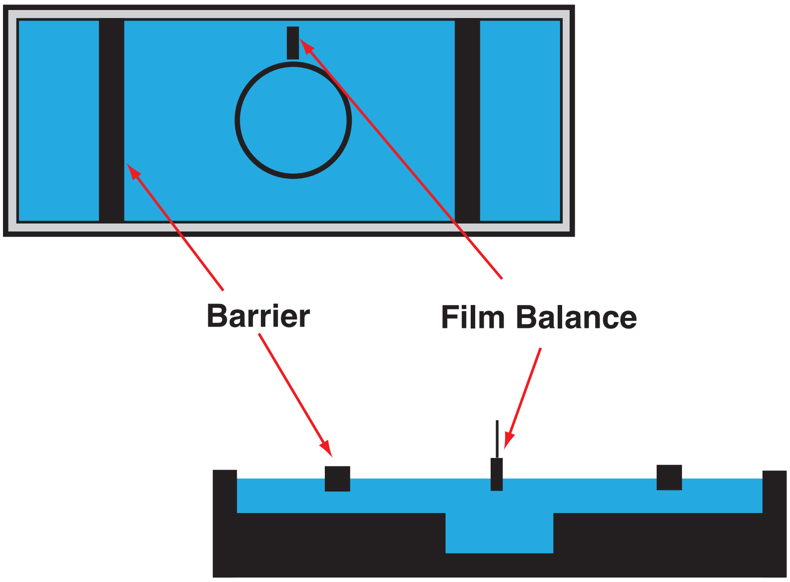

Figure 3.4.: Schematic illustration of a Langmuir trough with film balance.(Top: top view, bottom: side view)

Fig. 3.4 shows a schematic illustration of the Langmuir trough. The absolute surface area is at its maximum with 201.6 cm^2 and can be compressed to a minimum of 18.2 cm^2 by converging the barriers. The subphase height within the teflon well is only a few millimeters except for the central cylindric cavity that allows for complete submerging of substrates up to a height of about 2 cm.

Peltier elements within the bottom of the trough facilitate temperature control and stability of the subphase.

3.2.1. Film preparation

For the LB films used in this thesis eicosanoic acid ($C_{20}H_{40}O_2$), also called arachidic acid, has been used. Eicosanoic acid is a saturated fatty acid with a long, straight 20-carbon chain. The molecule is amphiphilic due to the hydrophobic chain and the hydrophilic acid moiety.

To ensure even distribution on the subphase the eicosanoic acid is dissolved in chloroform and then spread using a *μl-Hamilton* syringe. Volume and concentration of the solution have to be calculated according to the trough surface, in a way that the molecules are widely spread before compression and densely packed after contracting the barriers. This results in a typical concentration of 1 mmol/L of eicosanoic acid in chloroform and the use of 70 μL of this solution for one experiment.

After the solution is spread, the system is given typically 5 - 10 minutes in which it equilibrates and the solvent evaporates. Afterwards compression is started using a small motor speed, resulting in a maximal compression after 20 - 30 minutes. During this compression an isotherm is recorded by the PC system.

For further stabilization and denser packing of the eicosanoic acid molecules the subphase may be varied. For the experiments performed in the context of this thesis a subphase containing Ca^{2+} as counter ions has been used. To this end, a solution of typically 5 mmol/L calcium chloride ($CaCl_2$) in deionized water (Millipore system, resistivity $>18M\Omega/cm$) has been prepared. The pH of the subphase has been adjusted to 8.5 by adding small amounts from a NaOH solution.

3.2.2. Substrate preparation

The substrate used to create a LB monolayer were commercial microscope glass slides (0.5 mm tickles, 1 x 1 cm^2, *Plano GmbH*). These substrates have been sonicated first in ethanol and then in propan-2-ol for several minutes, respectively, prior to coating.

Substrates were rinsed directly before use or rinsed and stored under propan-2-ol to avoid contamination. To remove residual alcohol before coating, the substrate was allowed to dry in air for a few minutes or blown dry in a stream of high purity argon.

3.2.3. Film transfer

To transfer the molecular layer created in the trough to a glass substrate the dipping device has been used. To achieve a film transfer of a molecular monolayer the substrate has to be immerged into the subphase, prior to preparing the film as described above.

After the solvent has evaporated and the molecules were given time to equilibrate, compression starts. At a desired final pressure compression is stopped and the film is again allowed to equilibrate for several minutes before it is transferred onto the glass slide.

To ensure a steady film transfer a custom made magnetic clip would securely attach the glass slide to the dipping device. The film would be transferred at a constant surface pressure and a constant dipping speed of about 3 mm/min.

Subsequently, the coated glass slides are dried in air for at least one day to ensure the removal of residual water within the film.

3.3. Octadecyltrichlorosilane

The other major sample system used for this thesis is based on the molecule n-octadecyltrichlorosilane (OTS, $C_{18}H_{37}Cl_3Si$). For sample preparation again commercial microscope glass slides (0.5 mm tickles, 1 x 1 cm^2, *Plano GmbH*) have been used and initially cleaned by sonication for about 15 minutes in ethanol and subsequently immersed into a hot mixture (3:1) of concentrated H_2SO_4 and H_2O_2 for 45 minutes.

This strongly oxidizing solution[4] removes organic contaminations from the sample surface. Furthermore, it creates a hydrophilic surface with a high density of hydroxyl groups necessarily required for a proper binding of the OTS monolayer.

Prior to coating the cleaned samples were rinsed with deionized water (Millipore system, resistivity $>18\text{M}\Omega/\text{cm}$) several times and blown dry with a stream of high purity argon.

The subsequent OTS coating was carried out in a glove box under dry argon atmosphere to prevent the silane molecules from hydrolyzation. The samples have been immersed into the coating solution (1 mmol/L of n-octadecyltrichlorosilane in toluene (p.a. grade, used as provided, water content $<0.001\%$) for at least 20 hours at a temperature of 7 °C. Terminatory, the samples have been rinsed with toluene

---

[4] also known as: Caro's acid

and ethanol and then been dried in a stream of high purity argon.

3.4. Chemicals

Table 3.1.: Chemicals used

Name	Purity	Supplier
Argon (Ar)	high purity	Air Liquide Deutschland GmbH
Calcium chloride ($CaCl_2$)	$\geq$ 94%, dehydrate	Carl Roth GmbH & Co. KG
Choroform	analytical reagent grade	Fisher Scientific UK Ltd
Eicosanoic Acid ($C_{19}H_{39}COOH$)	analytical reagent grade	Sigma Aldrich
Eicosanoic-20,20,20-d_3 Acid (D_3C-$C_{18}H_{36}COOH$)	99.2 atom % D	CDN Isotopes
Ethanol absolute	analytical reagent grade	VWR International GmbH
Hydrogen peroxide	30% p.A.	AppliChem GmbH
n-Octadecyltrichlorosilane ($C_{18}H_{37}Cl_3Si$)	$<$ 3% C_{18} isomers	ABCR GmbH & Co. KG
Propan-2-ol	analytical reagent grade	VWR International GmbH
Sulfuric acid	S.G. 1.83 ($>$ 95%)	Fisher Scientific UK Ltd
Toluene	for analysis, ACS	Acros Organics, USA

4. Results

In this chapter the results of this thesis will be presented, starting with a peak assignment and analyzing of the SFG spectra in section 4.1. In section 4.2 results of temperature dependent experiments will be shown and discussed, followed by an orientational analysis in section 4.3. Finally results are summarized in section 4.4 accompanied by a short outlook (section 4.5).

4.1. Peak assignment

As the majority of conclusions in this thesis are deduced from SFG spectra, this section is centered around peak assignment and general presentation of sample spectra.

Fig. 4.1 depicts SFG spectra of an OTS coated glass samples recorded at room temperature. The different spectra correspond to different polarization combinations used in the experiments. The polarization combinations are denoted with respect to increasing wavelength (sum/vis/IR) as discussed earlier.

All lines that appear in the shown spectral region may be associated with C-H stretching vibrations of closely packed alkyl chains in organic monolayers. Therefore the peak assignment done for OTS largely holds true for arachidic acid, too.

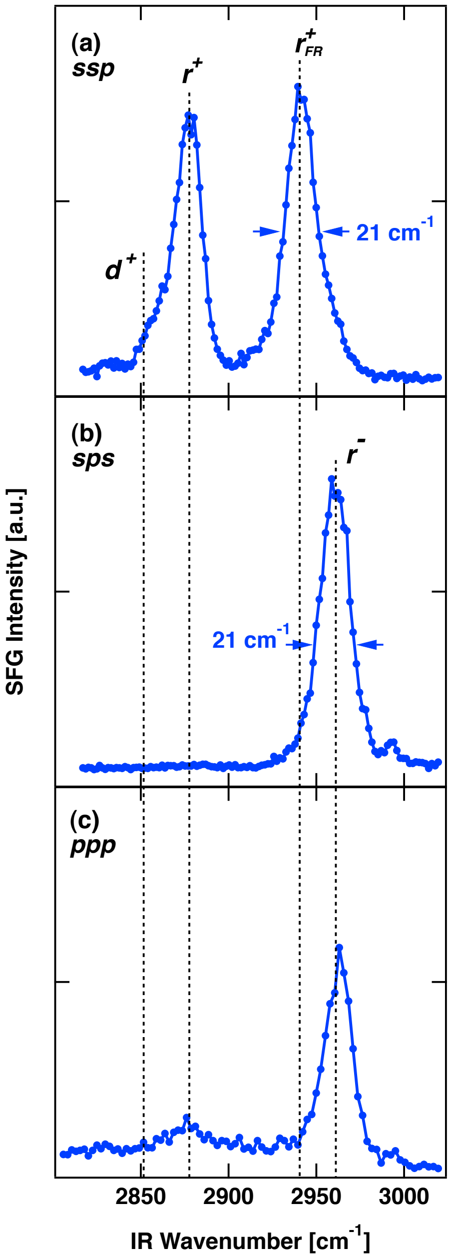

Figure 4.1.: SFG spectra of OTS coated glass at room temperature recorded using the three polarization combinations, (a) ssp, (b) sps, and (c) ppp.

The SFG spectrum shown in Fig. 4.1 (a) (*ssp*) exhibits two strong resonant features located at 2878 and 2941 cm^{-1} as well as a minor feature at 2851 cm^{-1} apparent as a subtle shoulder. The peaks at 2878 and 2941 cm^{-1} can be assigned to the symmetric stretching vibration of the terminal methyl group (r^+) which is split due to a Fermi resonance ($r^+{}_{\mathrm{FR}}$), manifesting itself as an overtone or combination mode of a bending vibration. The subtle shoulder at 2851 cm^{-1} is a contribution from the symmetric stretching modes (d^+) of the methylene (=CH$_2$) groups.

In agreement with the selection rules of sum-frequency generation spectroscopy the vibrational modes of the methylene groups are expected to cause only weak lines in an SFG spectrum, because their dipole moment is almost perpendicular to the surface normal and their nearly centrosymmetric arrangement in an all-*trans* configurated alkyl chain environment [60]. Deviation from this centrosymmetric arrangement may be caused by the slightly different physical environment at the chain ends near either the terminal methyl group or the siloxane anchor or due to the presence of gauche defects.

The influence of the physical environment may lead to a spectral shift of about 6 cm^{-1}, as reported by *Nihonyanagi et al.* [61] and *Chow et al.* [62] using a high-resolution sum-frequency generation technique. As the there employed spectral resolution is beyond the scope of the system used here, there will be no differentiation between this effect and the influence of gauche defects on the signal strength of the d^+-line in further discussion.

The antisymmetric stretching vibration of the terminal methyl group (r^-) appears at 2962 cm^{-1} and can only be observed in the *sps* and *ppp* spectra (Fig. 4.1 (b) and (c)). Additionally, one small peak appears at 2878 cm^{-1} in the *ppp* spectrum, which can be assigned to the symmetric stretching vibration of the terminal methyl group (r^+).

In contrast to the *ssp* spectrum (Fig. 4.1 (a)), the r^+-mode contributes only little in the *ppp* spectrum and the other line from the Fermi resonance is not observed here.

The distinctly different appearance of spectra recorded in diverse polarization combinations is to be expected, since all spectral, orientational and polarization information is contained in $\chi^{(2)}_{eff}$, which in turn dependents on the angles of incidence of light, as pointed out by *Wang et al.* [63]. As the incidence angles in the laser setup used here are fixed, it is impossible to have the maximal peak intensity for each line in every given polarization combination.

For that reason it is not astonishing that the *sps* spectrum (Fig. 4.1 (b)) does not reveal the r^+-mode. The appearance of a distinct r^--mode may be related to the IR excitation in the *s*-plane. This is plausible in consideration of the tilted end groups with respect to the surface normal. With a net transition dipole moment parallel to the surface plane the symmetric stretch (r^+) is suppressed, while the antisymmetric stretch (r^-) may yet be excited.

The line widths (FWHM) are about 21 cm^{-1} and thus significantly broader than the bandwidth of the IR laser with $\approx$9 cm^{-1}. Reasons for this may be an inhomogeneous broadening of lines due to a multitude of molecular environments present in condensed monolayers, which are then averaged by the probe beam [64]. Additionally an overlap of different vibrational modes, as suggested by high-resolution studies mentioned above [62], may also contribute to the line broadening. *Chow et al.* are able to identify a splitting of the r^+_{FR}-mode by 6 cm^{-1} in their work [62].

While the spectral resolution of the system used for the experiments presented here is not sufficient to distinguish between such a splitting, it is important for the considerations with respect to peak fitting. Therefore some general ideas and approaches to the peak fitting procedure will be discussed here, while the exact details will be given later in association with the respective experiments.

The most common mathematical description for a peak in an SFG spectrum is a *Lorentzian* profile (see eq. 2.9) [62, 61] or in case of inhomogeneous line broadening a *Gaussian* profile [64]. Therefore initial fitting attempts have been done on the basis of Gaussian functions.

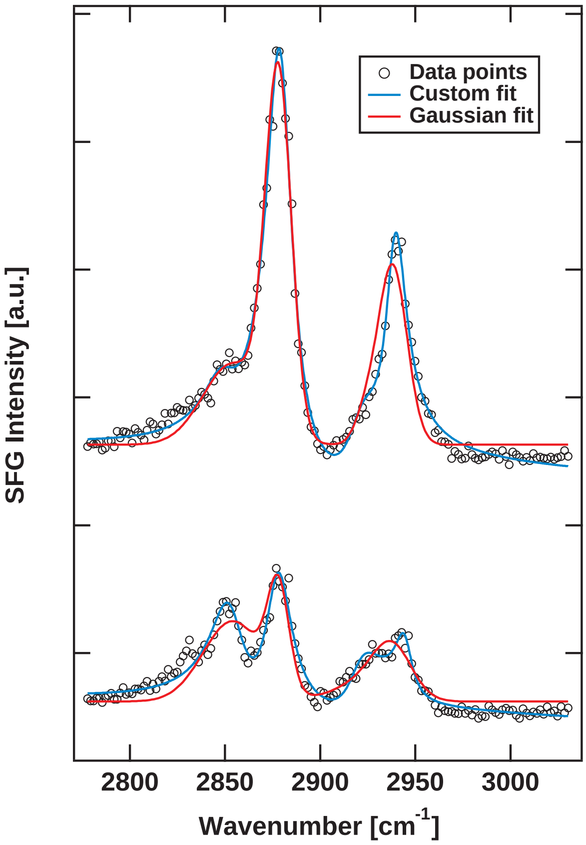

Figure 4.2.: Two exemplary SFG spectra recorded in *ssp*-polarization combination. Data points are shown as open black circles, a Gaussian fit (red line) as well as a custom fit (blue line) are added. Further explanation in the text.

Looking at Fig. 4.2 it becomes apparent that a Gaussian fit (red line) is an inadequate description for the shown data points (open black circles) of the two exemplary SFG spectra. Even though there might be some inhomogeneous broadening of the lines, the Gaussian profile does not describe the data points well. As a result other fit functions have been tried. Lorentzian profiles, while mostly fitting the data better than Gaussian profiles, are also not ideal for some peaks. A better agreement between data points and fit function can be achieved when using a *Voigt* profile. The Voigt profile is a line profile resulting from the convolution of a Lorentzian and Gaussian profile. Yet, fitting the data to a Voigt profile results in a multitude of fit parameters. Several of these parameters cannot be brought into connection with physical phenomena in the context of SFG spectra.

Therefore the peak fitting done in this work has been performed by using a custom fit function (blue lines in Fig. 4.2), as proposed by *Vidal et al.* [42] based on eq. 2.11. Employing this equation for peak fitting has the combined advantage of resulting in physically reasonable parameters and being able to describe phase effects between peaks, when necessary.

As some points in the exact fitting procedure are varied for the respective systems studied, details are given when these are presented. In general it was advantageous to use a spectrum where a specific peak was prominent to identify the central frequency for the line and then use this line position as a fixed value for the fitting of further spectra. As a result it was possible to find reasonable parameters even for spectra with a poor S/N ratio.

Apart from the intensity variation, due to polarization dependence, the peaks found following this approach correspond well with vibrational frequencies found in former SFG studies on OTS monolayers on glass or silica substrates [61, 62, 65, 66, 67, 68, 69].

Table 4.1.: Peak assignment for the spectra presented in Fig. 4.1

Stretching vibration		ω **[cm^{-1}]**
Symmetric stretch -CH_3	r^+, r^+_{FR}	2878, 2941
Antisymmetric stretch -CH_3	r^-	2962
Symmetric stretch =CH_2	d^+	2851

A similar approach can be made for the interpretation of SFG spectra of arachidic acid monolayers. Fig. 4.3 shows a typical spectrum of a Ca-Arachidate (CaA) monolayer at a sample temperature of 370 K.

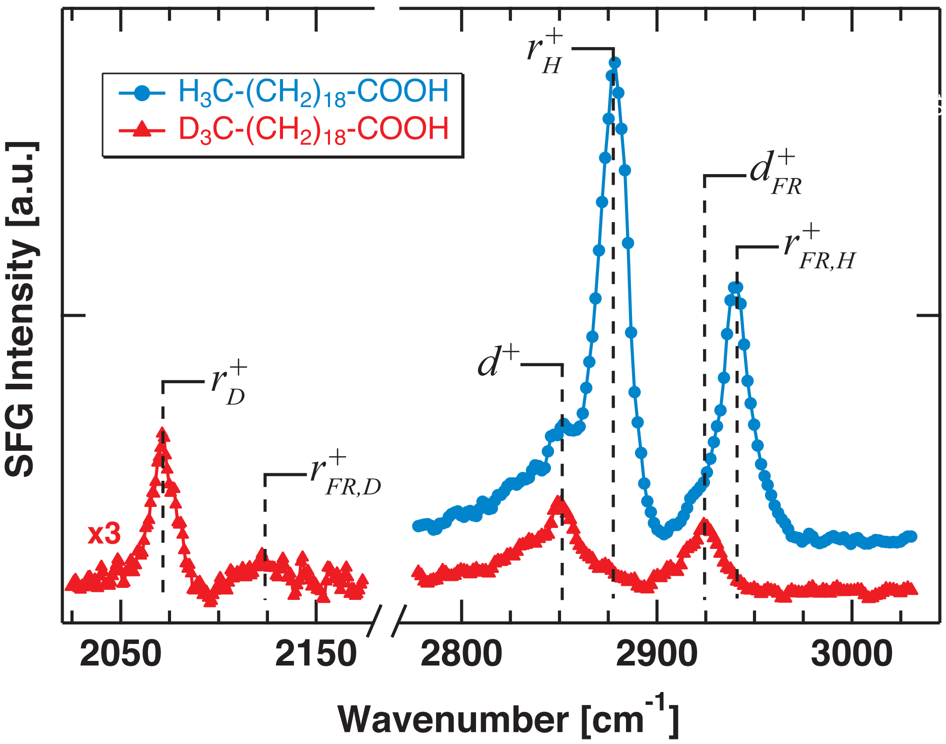

Figure 4.3.: SFG spectra of Ca-Arachidate monolayers on glass composed of arachidic acid (blue circles) and arachidic-20,20,20-d$_3$ acid (red triangles) at a sample temperature of 370 K. Spectra were recorded in *ssp*-polarization combination.

However, some adjustments have been made in the case of CaA. On the one hand the *ppp* and *sps* polarization combinations reveal no relevant spectroscopic features in the observed area, therefore only the *ssp* spectrum is shown here. As all the relevant lines used for later data evaluation are exhibited in the *ssp* spectra, the rest may be neglected without deficiency.

On the other hand spectroscopic information has been added by probing not only arachidic acid, but also arachidic-20,20,20-d$_3$ acid, a specially deuterated isotopologue of the molecule. The substance used here was accurately defined to have only the terminal methyl group (-CH$_3$) replaced by the respective deuterated methyl group (-CD$_3$). The chain's methylene moieties (=CH$_2$) are unmodified in the process.

When looking at the arachidic acid spectrum (blue circles) in Fig. 4.3 it exhibits two major features located at 2878 and 2938 cm^{-1}, which are, similar to the case of OTS, attributed to the symmetric stretching vibration (r_H^+) of the terminal methyl group, split due to a Fermi resonance ($r_{FR,H}^+$). At the respective red wings of these features peaks apparent as shoulders can be found at 2854 and 2924 cm^{-1}. These resonances may be assigned to the symmetric stretching mode (d^+) and the respective Fermi resonance (d_{FR}^+) of the methylene groups. Other studies of long-chain aliphatic LB-films on various substrates find comparable results for the mentioned frequencies [52, 70, 71, 72].

Apart from the d_{FR}^+-line the spectral region between 2910 and 2930 cm^{-1} may also show the antisymmetric stretching vibration d^- of the methylene groups. Since the contribution of this antisymmetric mode is negligible in the polarization combination used here (*ssp*) [73, 63], it is more likely that the observed line at 2924 cm^{-1} is solely due to the Fermi resonance (d_{FR}^+). This assignment is further corroborated by the fact that no line was detected around 2920 cm^{-1} when recording in *ppp* polarization combination. The frequency of 2924 cm^{-1} for the d_{FR}^+-line is also in good agreement with surface-enhanced Raman scattering (SERS) measurements [74].

It should be noted that the spectra shown in Fig. 4.3 are in contrast to the ones shown for OTS above, recorded at a temperature of 370 K. The higher temperature leads to a more prominent appearance of the d-lines, making an assignment easier. The underlaying reasons for this behavior will be discussed in greater detail in a following section.

The spectrum of the deuterated arachidic acid (red triangles) in Fig. 4.3 looks distinctly different to the one of the not deuterated version. While the chemical properties of both substances do not differ, the varying masses of hydrogen and deuterium lead to an altered spectral response. It is therefore not surprising that the symmetric stretching vibration (r_D^+) of the deuterated terminal group is shifted to a frequency of 2071 cm^{-1}.

The observed redshift corresponds with the ratio of the reduced masses (μ) for CH and CD, thereby introducing a factor of about 1/1.37 when comparing the frequencies (ω) of r_H^+ and r_D^+.

$$\frac{\omega_1}{\omega_2} \propto \sqrt{\frac{\mu_2}{\mu_1}} \tag{4.1}$$

and

$$\mu = \frac{m_1 \cdot m_2}{m_1 + m_2} \tag{4.2}$$

This finding is also backed by infrared spectra of crystalline deuterated n-alkanes recorded at low temperature by *MacPhail et al.* [73], who find the r_D^+-mode at 2073 cm^{-1}.

Unfortunately the intensity of the SFG signal at lower wave numbers is inherently smaller due to a reduced pulse power[1] of the laser system in this spectral region. It is therefore difficult to identify the corresponding feature of the Fermi resonance $r_{FR,D}^+$. Even though a fuzzy peak centered around 2124 cm^{-1} may be distinguished from the noise level and attributed to the $r_{FR,D}^+$-line.

As there has been no alternation of the chain's methylene groups, their spectral frequencies are not shifted. The d^+-line is centered around 2854 cm^{-1} and the d_{FR}^+-line around 2924 cm^{-1}, as observed in the case of arachidic acid. Still, due to the absence of the terminal methyl group features in this spectral region, both d-lines are easier to identify.

Table 4.2.: Peak assignment for the spectra presented in Fig. 4.3

Stretching vibration		ω **[cm^{-1}]**
Symmetric stretch -CD$_3$	$r_D^+, r_{FR,D}^+$	2071, 2124
Symmetric stretch -CH$_3$	$r_H^+, r_{FR,H}^+$	2878, 2938
Symmetric stretch =CH$_2$	d^+, d_{FR}^+	2854, 2924

---

[1] The pulse power is reduced by about 50% at wave numbers around 2000 cm^{-1}, when compared to wave numbers around 3000 cm^{-1}.

4.2. Experiments at elevated temperature

4.2.1. Results for the OTS system

After having established a general approach to the interpretation of SFG spectra, this section will focus on the core propositions of this thesis related to experiments under the influence of elevated temperature. In this regard SFG spectra shall be analyzed with respect to changes due to temperature modification. Possible interpretations for the structural change on a molecular level can be discussed on that basis.

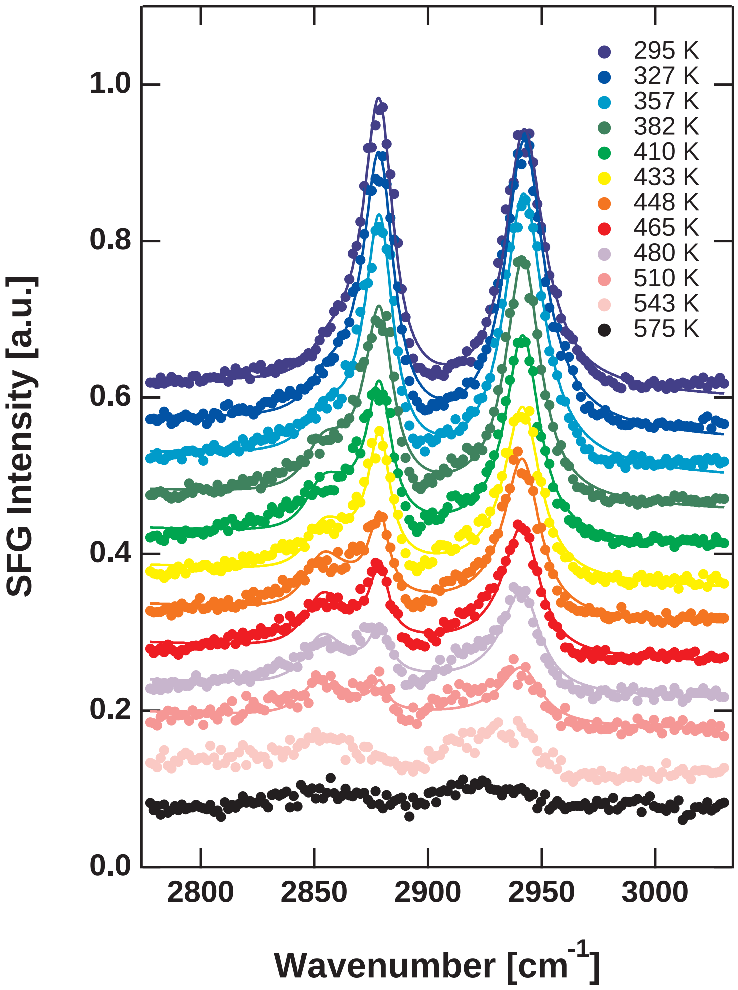

Figure 4.4.: SFG spectra of an OTS covered glass substrate at various temperatures recorded under ambient conditions using *ssp* polarization combination. The solid lines are fits using eq. 2.11. The baselines are separated by a vertical offset.

To this end experiments have been conducted, in which SFG spectra have been recorded in the same spectral region as discussed before. Between experiments the sample temperature has been increased from 300 K to 575 K in increments of 20 to 40 K. Fig. 4.4 depicts the resulting SFG spectra at various temperatures for an OTS system on a glass substrate. The spectra have been recorded in *ssp* polarization combination. There are neither significant changes to the line positions nor width upon heating. The baseline caused by green stray light was close to zero regardless of temperature.

The spectra shown in Fig. 4.4 are separated by a vertical offset in order to make distinction easier. Data is gathered by tuning the IR light with a step size of 2 nm. Each point shown in the figure corresponds to an averaging of 300 values recorded for each step. This way shot-to-shot fluctuation in laser intensity may be compensated. All spectra were fitted to eq. 2.11 for deconvolution analysis of the peaks employing a user defined fitting routine. Note, that it was refrained from fitting spectra recorded at temperatures 543 and 575 K in this way as the signal-to-noise ratio in these cases does not allow for a reasonable analysis.

The parameter for the peak strength A_ν is scaled with respect to the maximum intensity of the r^+-mode. No non-linear background signal from the amorphous glass surface could be detected at any temperature, interference effects between the background and a potentially phase shifted vibrational resonances therefore do not need to be considered in the analysis.

Instead the phase ξ was referenced to the r^+-mode, for which it was set to zero. The phases ξ were constrained to values between 0 and π to obtain a unique set of solutions. The vibrational frequencies ω were fixed at the values summarized in table 4.1, the damping constants Γ were constrained to correspond to a reasonable line widths between the bandwidth of the laser system (9 cm^{-1}) as a lower limit and 22 cm^{-1} as an upper limit, representing a typical value to account for line broadening [61]. In eq. 2.11 the line width (FWHM) is given by 2Γ.

From the fit results, shown in Fig. 4.4, two trends are evident. The room temperature spectrum (topmost curve) reflects the sample surface after the coating process, prior to any thermal treatment. The r^+ and r^+_{FR}-modes dominate the spectrum here, while the d^+-mode is just barely visible as a dent on the red wing of the r^+ peak. This picture changes markedly with increasing sample temperature. While the intensity of the methyl group declines, the d^+ contribution first becomes apparent as a prominent shoulder in the r^+ peak until it finally emerges as a distinct peak of comparable size.

These trends are stopped at sample temperatures between 543 and 575 K, where the SFG signal is lost, indicating significant degradation of the monolayer. This degradation can be explained by thermal decomposition as described by *Safarik and Strausz* [75], following a homolytic scission of a C-C bond in the organic chain producing two alkyl radicals.

Kluth et al., in this context, find that alkylsiloxane self-assembled monolayers decompose at temperatures above 740 K in vacuum, primarily through the cleavage of C-C bonds [76]. A better agreement to the data presented here can be found by looking at the work of *Kim et al.*, as they find a stability of self-assembled alkylsiloxane monolayers up to 500 K in air [77]. In their work, they also propose decomposition, as described above [75], by cleavage of C-C bonds starting at about 520 K.

The decomposition temperature of the alkylsiloxane monolayers in air is about 200 K lower than that in vacuum, indicating that O_2 and H_2O in air may accelerate the propagation steps [77].

As the decomposition mechanism above the 500 K mark is well explained, it will not be the subject of discussion within the framework of this thesis.

While the overall loss of SFG signal due to thermal decomposition may be understood quite intuitively, it does not account for the shift in the intensity ratio of the different lines of the spectrum. This effect can, in accordance with SFG selections rules, be related to a gain in defects in the all-*trans* chains accompanied by breaking of local centrosymmetry.

As chain degradation only starts at higher temperatures these defects are not the product of C-C bond cleavage, but rather the consequence of twists in the alkyl chains. These twists are leading to a different conformations and can be named in analogy to alkanes *anti* and *gauche* configuration, see Fig. 4.5.

Therefore, in the context of this thesis a twist in an alkyl chain will also be referred to as a *'gauche defect'*. The vibrational modes of the methylene groups become SFG active upon conformational changes since the local inversion symmetry of the alkyl chain is broken. This leads to a strengthening of the methylene d^+-mode in the SFG spectra with an increasing density of conformational defects. The parameter $A(d^+)$ reflects this evolution.

Yet, it has to be taken into account that two competitive effects on the SFG signal intensity are observed here. On the one hand the d^+-line is intensified by a gain in defect sites with rising temperature, but on the other hand the overall SFG

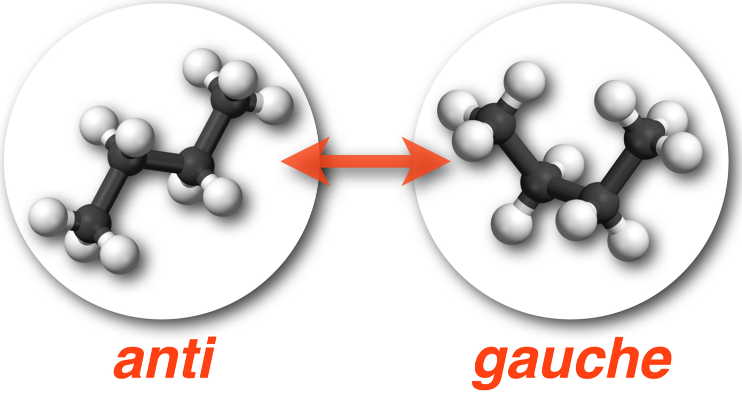

Figure 4.5.: Schematic illustration of *anti* and *gauche* configuration for a butane molecule.

intensity decreases due to a stronger isotropy of the sample facilitated by the same temperature increase. To compensate this problem not only the $A(d^+)$ parameter, but rather the intensity ratio $A(d^+)/A(r^+)$ is taken into account. This approach has successfully been used for comparable systems [78, 79] as well as OTS before [66], though in the context of monolayer growth and solvent effects.

The underlying idea is to use the $A(r^+)$ parameter to account for thermally induced variations of the signal intensity, which do not primarily arise from conformational disorder, e.g. a variation in peak intensity due to more tilted alkyl chains, thereby separating the two competitive effects. Although the methyl symmetric stretch intensity is split by a Fermi resonance to yield the intensity in two peaks, only the one at 2878 cm^{-1} will be used in this consideration, as it is the approach utilized in the literature. This approach is legitimate, as splitting due to a Fermi resonance does not change the ratio under consideration for this purpose. Furthermore, mixing between the two states should not be dependent on methyl group orientation based on symmetry considerations [79]. Since r^+ and r^+_{FR} are in phase and of similar strength in the spectra, no additional gain in information is to be expected.

Both parameters, $A(d^+)$ and $A(r^+)$, can be extracted from the fits to the *ssp*-spectra. The ratio $A(d^+)/A(r^+)$ reflects the evolution of conformational defects within the monolayer since A is proportional to the number of oscillators probed. Thus, this ratio can be used for evaluating the given conformational order at varied temperatures.

For an ideally packed layer of molecules in all-*trans* configuration this ratio would be expected to be close to zero, as in a crystal-like environment the methylene

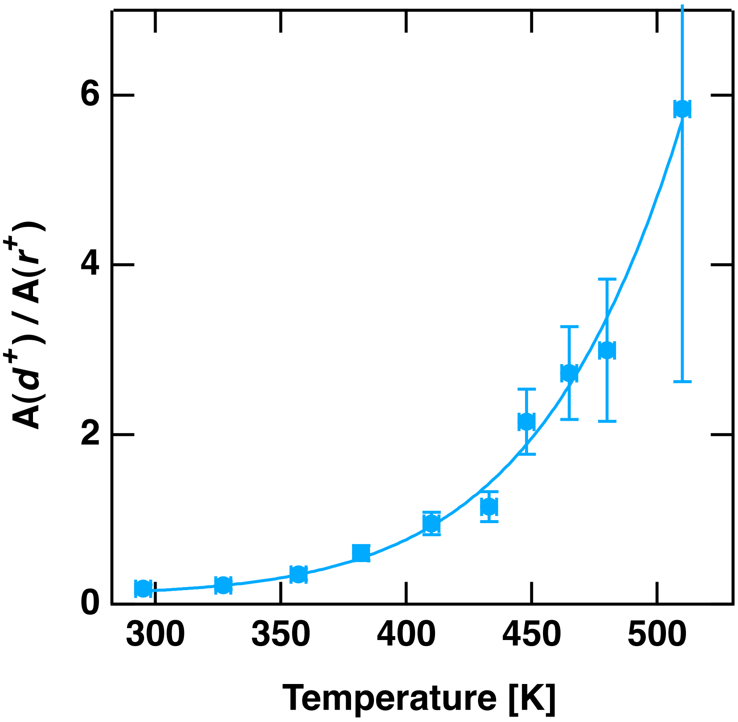

Figure 4.6.: Ratio of the sum-frequency transition strengths of the d^+ and r^+-lines. $A(d^+)/A(r^+)$ determined by fitting the *ssp*-spectra (Fig. 4.4) as function of temperature. At higher temperatures the error margins are larger due to a smaller SFG signal and therefore a larger uncertainty in the fits to the spectra.

groups are almost perfectly centrosymmetric. Experimentally, this assumption is not confirmed. When looking at Fig. 4.6 a ratio of $A(d^+)/A(r^+) \approx 0.2$ can be found for the sample system, even before heating. This may result from a significant contribution of the d^+-peak in the spectrum, indicating a non-zero degree of chain disorder.

This can be put down to a non-ideal crystal packing as part of the self-assembly process forming an OTS monolayer, resulting in a d^+ contribution. This growth, as described earlier, may be seen as a combination of "uniform" and "island-type" growth model [16], for the samples used in this work. The island-type growth model in particular assumes a pre-polymerization of OTS molecules in solution, facilitated by water. These pre-polymerized aggregates cannot be expected to have a long-range order, as they are in a liquid environment. Once the aggregates are grafted to the substrate covalent bonds are formed [15] and mobility is lost. During this process it is not unreasonable to expect that imperfections in the crystal structure are "pinned" by the binding event. Atomic force microscopy (AFM) studies [80] and model calculations [17] done earlier by our group for a similar system corroborate the idea of defects in the monolayer, incompatible to the image of an uniform crystal. The approach in these studies is centered around the fact that siloxane oligomers may also be held by rather weak interactions, such as hydrogen bonds [14]. In the course of reaction weak bound parts may then leave the substrate, before grafting or lateral cross-linking takes place. The void sites created thereby can be seen as pinhole defects in the structure. The size of these defects range from the μm to nm regime in the process of monolayer formation [80].

In contrast to other SAM systems, such as thiols on gold, the presence of an irreversible covalent cross-linking step - while ensuring a chemical and mechanical robustness on a variety of substrates - does not allow for annealing of the structure or assuming the epitaxial arrangement of the substrate lattice [81, 7].

Furthermore, grazing incidence X-ray diffraction (GIXD) experiments carried out by *Tidswell et al.* [20] reveal no evidence for a truly crystalline structure [7]. The polarity and viscosity of the solvent is also discussed to have a certain influence on the homogeneity of the monolayer [82].

As a result, temperature induced *gauche* defects may already be energetically accessible at room temperature. Unfortunately, vibrational sum-frequency generation spectroscopy cannot distinguish between temperature- and pinhole-induced effects, as it is only sensitive to symmetry.

In contrast a change form $A(d^+)/A(r^+)$ initially ≈ 0.2 to almost 6, as apparent in Fig 4.6, indicates a dramatic change in the molecular order, by adding *gauche* defects. Here sum-frequency generation spectroscopy is a method capable of revealing a phenomenon, where other methods such as AFM, contact angle measurement or XPS are nonsensitive.

A phase transition, as observed by *Koga et al.* [83], utilizing GIXD to differentiate between a hexagonal and an amorphous state at 318 K cannot be deduced from the data presented here. Yet, these results do not have to be in conflict with the findings here, as a phase transition is not necessarily accompanied by a higher defect density nor a change in molecular tilt angle.

Nevertheless, a change in the lateral order of the alkyl backbone is linked to a variation of lattice constants, raising the question whether the packing density of the molecules comprising the monolayer has an influence on the creation of *gauche* defects.

Another approach for data analysis on the basis of $A(d^+)/A(r^+)$ is imaginable. Thermodynamical quantities, deduced from Boltzmann-type statistics, are accessible, when assuming that $A(d^+)/A(r^+)$ reflects an equilibrium constant K for the ratio of CH_2 (*gauche*) to CH_2 (*anti*) oscillators of the molecules at the surface:

$$K = \frac{CH_2(gauche)}{CH_2(anti)} \tag{4.3}$$

In this context it is important to remember that Boltzmann-type statistics of this type may only be employed for systems in thermodynamic equilibrium. If this requirement is met, it is justified to assume the given ratio as an expression for the microscopical conformational disorder.

Considering this, experiments have been conducted to ascertain, whether the formation of *gauche* defects, as observed in the spectra, is reversible. Finding a reversibility of the reaction within a reasonable time frame would corroborate a state of thermodynamic equilibrium. To this end a modified experiment has been executed. Here, a freshly prepared substrate coated by organic monolayer was heated from room temperature to a given end temperature, before being allowed to cool back to room temperature in each case. During this process the SFG intensity of the strongest line in the spectrum (terminal -CH_3, r^+) was monitored, thereby giving a continuous feedback while heating. Apart from equilibrium considerations, the reversibility of the thermally induced chain disorder may also be an important aspect in view of applications, where a distinct orientation of the head groups for functionalization purposes is required.

The data for two distinct maximum temperatures, namely 358 K and 442 K, are exemplarily shown in Fig. 4.7.

The figure shows the temperature development, governed by the experimental conditions as well as the response signal of the oscillators. Upon activation of the heating a rather quick increase in sample temperature is apparent, followed by a flattened ascent to the final temperature, due to the rather thick copper disc involved. Accordingly the temperature decrease, upon switching off the heating, follows a leisurely decline while copper disc and sample are cooling down. The SFG response signal, shown in the lower part of the figure, is depicted in normalized form against the intensity of the SFG signal before heating the sample. Temperature curves as

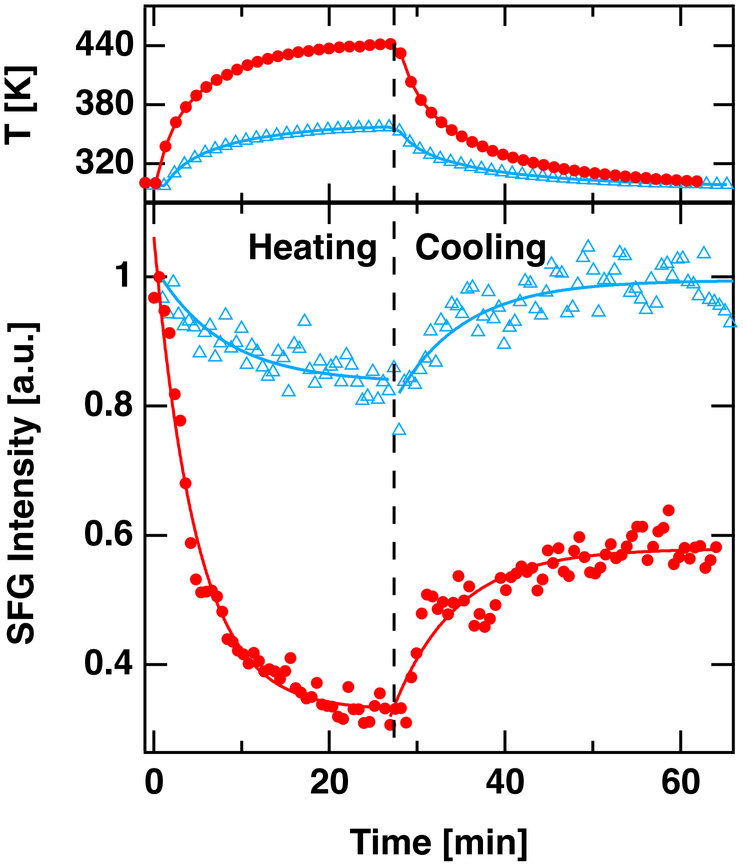

Figure 4.7.: Sample temperature (topmost graphs) and corresponding SFG intensity of the r^+-line at 2878 cm^{-1} (lower graphs) recorded in *ssp* polarization combination for two different end temperatures. The SFG intensities are normalized with respect to maximum intensity prior to heating. The solid lines are single exponential fits.

well as SFG response signals can be fitted satisfactorily using single exponential functions for both heating and cooling sections.

It can be expected that in both cases a drop in SFG intensity follows upon increase of temperature. This trend may be constituted due to both, an increase in chain disorder as well as more divergent distribution of molecular tilt angles.

Yet, distinctions for different end temperatures can be seen, when comparing the SFG response while cooling back to room temperature. In the case of the experiment with 358 K as a maximal temperature the SFG signal is completely recovered, once the sample is cooled back to room temperature, while in the 442 K experiment a recovery to less than 60% of the initial value can be observed.

For a more complete picture Fig. 4.8 shows a wider range of heating-cooling cycles; the presentation of temperature profiles has been omitted, as no differing trend could be observed.

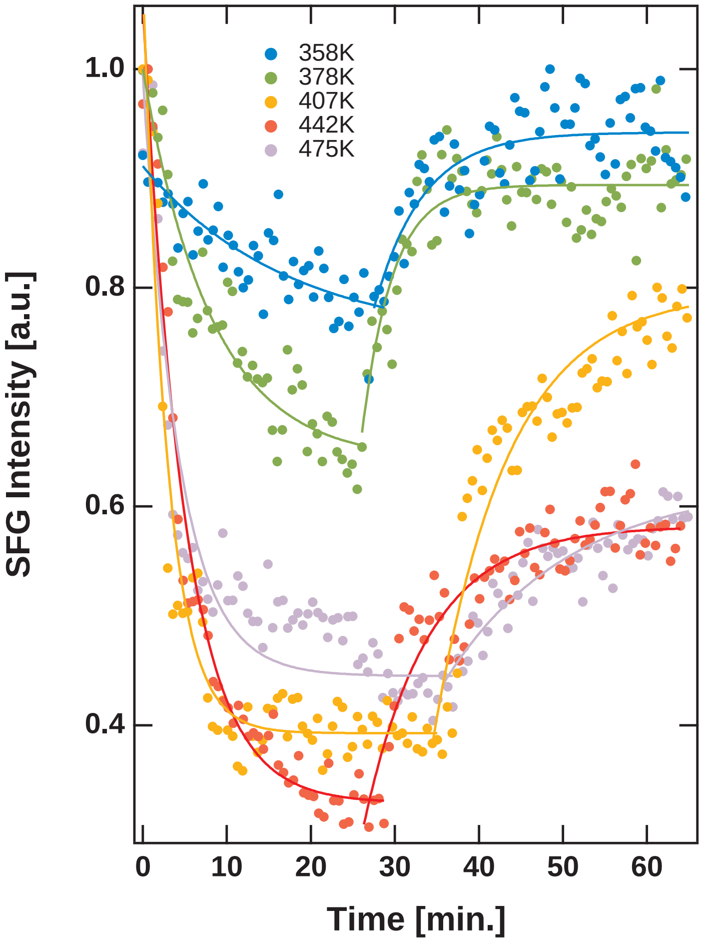

Figure 4.8.: SFG intensity of the r^+-line at 2878 cm^{-1} recorded in *ssp* polarization combination for different end temperatures. SFG intensities are normalized with respect to maximum intensity prior to heating. All solid lines are single exponential fits.

The presented data indicate that irreversible structural changes of the monolayer must be expected upon heating to higher temperatures. For further analysis a cut is assumed for temperatures below and above 410 K. The 407 K experiment reveals a signal recovery to almost 80% of the initial value, with a trend apparent for the fit that suggests even further recovery. Therefore it is justified to assume a reversible temperature regime up to heating to 410 K and an irreversible regime when applying higher temperatures.

While it is impossible, on the basis of this data alone, to derive what the exact microscopical impact is, a structural change appears plausible, as different heating experiments above the 410 K threshold result in a signal recovery to about 60%.

This clearly is in contrast to the assumption that oxidation might be starting at lower temperatures, as a complete signal loss without any recovery would be the consequence.

It is worth noting that the recovered SFG signal never exceeded the initial one, which was observed after sample preparation. This suggests that moderate heating cannot be used for annealing to reduce defects present after the wet chemical preparation of the monolayers. This finding is in good agreement with the reaction model for the composition of the OTS siloxane network. Covalent bonds and irreversible cross-linking do not allow for annealing, as mentioned above.

The described experiments show at least in part that it should be possible to employ Boltzmann-type statistics for the sample system presented here. Thermal equilibrium concerning the conformational changes is given, as the sample systems are homogeneously heated and held at the designated temperature for some time, before recording of the spectra. This assumption is supported by the fact that no changes in the SFG spectra could be observed, while holding the sample at a temperature in the range from 300 to 410 K for an extended timespan.

Under these conditions a reaction enthalpy $\Delta_R H$ can be calculated using a equilibrium constant K as defined in eq. 4.3 by applying the van't Hoff equation in the following form:

$$\frac{d\ ln\ K}{d\ (1/T)} = -\frac{\Delta_R H}{R} \tag{4.4}$$

The van't Hoff equation in chemical thermodynamics relates the change in the equilibrium constant K of a chemical equilibrium and the change in temperature T to the enthalpy change $\Delta_R H$ for the process. Thus, $\Delta_R H$ can be determined from the slope of a line fit in a so called van't Hoff plot ($ln\ K$ vs. $1/T$, see Fig. 4.9).

Following this approach $\Delta_R H$ is calculated to:

$$\begin{aligned} \Delta_R H &= -R\ \cdot\ slope \\ &= 14\ \pm\ 2\ kJ/mol \end{aligned} \tag{4.5}$$

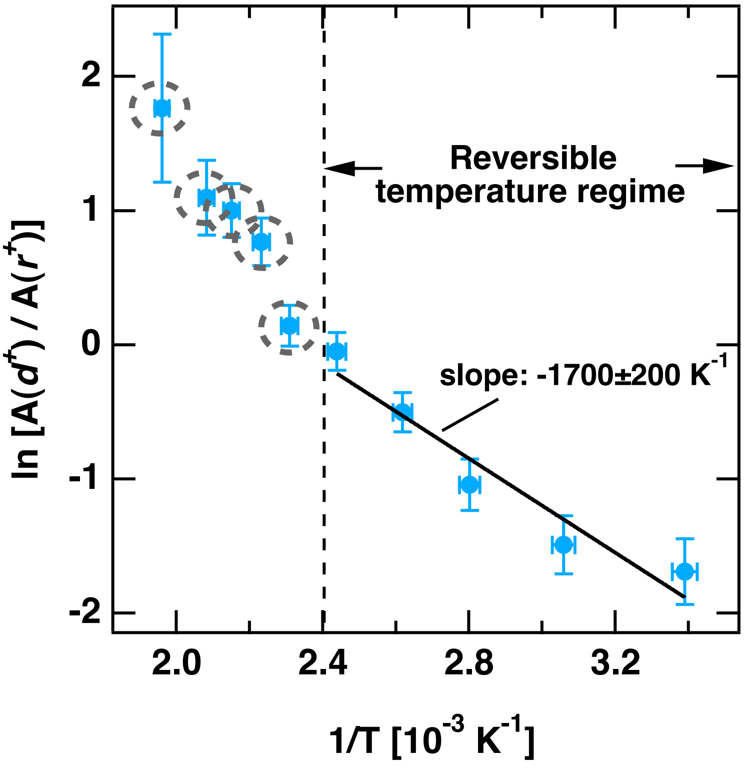

Figure 4.9.: Van't Hoff plot on the basis of the intensity ratio shown in Fig. 4.6. Data points marked by grey circles are excluded from the line fit, as they do not fall into the reversible temperature regime observed for the reaction.

Additional thermodynamic quantities may be derived. The reaction entropy $\Delta_R S$ is given by:

$$\Delta_R S = \frac{\Delta_R H}{T} + R \cdot \ln K(T) \tag{4.6}$$

The Gibbs free energy $\Delta_R G$ is then defined to be:

$$\Delta_R G = \Delta_R H - T \Delta_R S \tag{4.7}$$

However, using eq. 4.6 requires the knowledge of an exact K, as defined by eq. 4.3, whereas the ratio $A(d^+)/A(r^+)$ may possibly only represent a proportionality of K.

Orientational factors may have an impact on the ratio $A(d^+)/A(r^+)$, as discussed later. In spite of this a calculation based on eqs. 4.6 and 4.7 may be attempted. Interpretations of this kind have been done in the literature [84] before.

Using the reaction enthalpy $\Delta_R H$ gained through the van't Hoff plot an entropy change of $\Delta_R S = 32 \pm 5$ J/mol K can be deduced. This is in accordance with values found for common lipid monolayer with long saturated alkyl chains. For such a system in comparison the rotation of one alkyl group was found to be 5 kJ/mol for the enthalpy and 9 J/mol K for the entropy [85]. These quantities may serve as a lower limit, because a conformational transition must affect at least one C-C bond within the chain. As an upper limit the melting enthalpy and entropy could be used respectively, since the conformational order in the monolayer is not completely lost. Melting enthalpy values are found to be about 25-50 kJ/mol, while melting entropy for a lipid monolayer is in the range of 80-150 J/mol K [85].

These values fit surprisingly well. Both enthalpy and entropy fall in between the suggested limits, with a tendency to be nearer to the lower limit then to the upper one. This is probable, as *gauche* defect formation is easier related to a twist of a C-C bond than to a full melting process. Therefore, the pictured model concept and derived data are congruent. Further comparison underlines this idea, especially when considering the enthalpy values.

Gurau et al. [84] find a $\Delta_R H = 7.3$ kJ/mol for a system of octadecylamine monolayers spread on acidic salt solutions, also using SFG as a tool for observation and determining thermodynamic quantities in the described way. Their findings are of the same magnitude as the ones presented within the framework of this thesis and may be further compared to the simplest system imaginable in this context for classification. The transformation of gas phase butane from the staggered (*anti*, all-trans configuration) into the eclipsed (*gauche*) configuration represents the simplest analogy for the formation of a *gauche* defect within a long alkyl chain. A value of $\Delta_R H = 2.8$ kJ/mol was obtained spectroscopically [86] for this molecule. The fact that this value is significantly lower than the value of 14 kJ/mol found for the OTS system here does not surprise. Considering gaseous butane, van-der-Waals interactions between neighboring alkyl chains are completely neglected. The potential energy difference of both rotated states of a methylene group in an OTS monolayer should be larger, since the chains are immobilized and densely packed within the layer. Therefore, the value for gas phase butane can only serve as a lower limit. Yet, there should be no difference in orders of magnitude as the two cases are still comparable.

Connecting $\Delta_R H$, found here, with rather big values for $\Delta_R S$ results in a small Gibbs free energy $\Delta_R G$ in the range of 5 kJ/mol. A possible explanation is that a C-18 alkyl chain offers a large number of possible *trans/gauche* transitions. Hence, the number of configurations possibly realizing a *gauche* defect rises alongside the entropy, consequently squelching $\Delta_R G$.

In the context of *gauche* defect formation for the OTS systems observed in this work, especially the consideration of $\Delta_R H$ values is feasible. These values have the particular benefit to be obtained from the slope of the van't Hoff line fit and as a consequence are independent form the considerations of $A(d^+)/A(r^+)$ being exactly K or just proportional to K. This is important since the exact relation between K and *gauche* defect formation is not fully understood, as will be discussed in the next section. Therefore the calculation of $\Delta_R S$ and consequently $\Delta_R G$ on the basis of K is certainly subject to some error and may not be overestimated here.

4.2.2. Results for the Ca-Arachidate system

In a comparable approach Ca-Arachidate experiments have been analyzed.

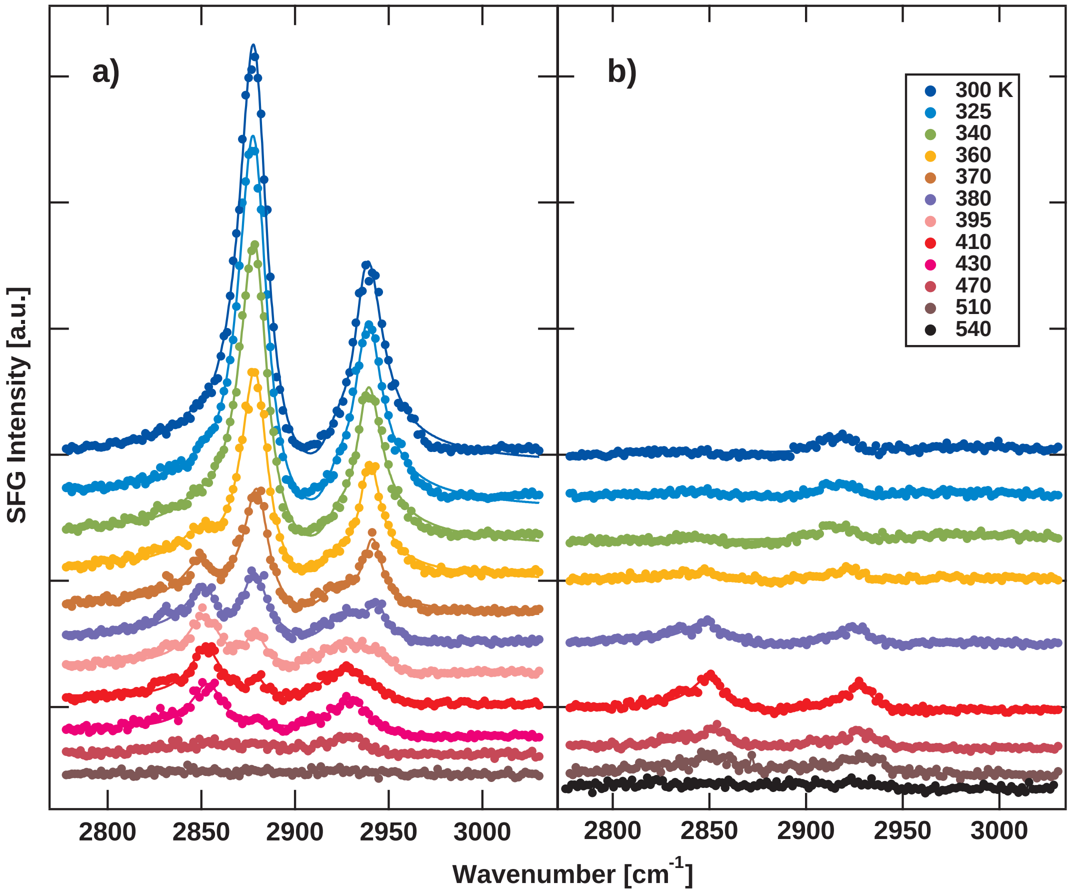

Figure 4.10.: SFG spectra of a glass substrate after deposition of a) Ca-Arachidate and b) Deutero-(20,20,20-d3)-Arachidate at various temperatures recorded under ambient conditions. All spectra were recorded using *ssp* polarization combination. The solid lines are fits using eq. 2.11. The baselines are separated by a vertical offset.

Figure 4.10 shows SFG spectra of both CaA (a) and d3-CaA (b) monolayers recorded at various sample temperatures. The presented data cover the same spectral region as the ones for OTS did. The same polarization combination (*ssp*) has been employed and the spectra show the same lines, namely the symmetric stretching mode of the terminal methyl group (r^+, r^+_{FR}) as well as the symmetric and antisymmetric stretching modes of the methylene moieties (d^+, d^+_{FR}). The temperature for different experiments was varied from 300 to 510 K in steps of 10 to 40 K. All spectra obtained in the process were fitted to eq. 2.11, the solid lines in Fig. 4.10 represent the respective fit results.

For deconvolution analysis the four lines mentioned above were assumed to contribute to the signal in the spectral region studied. The fitting parameters used were A_ν and Γ_ν, while $e^{i\xi}$ describes the phase relation between a resonance and the possible non-resonant background.

As no non-resonant background could be detected experimentally for the glass substrate used, eq. 2.11 can be simplified. With no non-resonant background $\chi^{(2)}_{NR}$ may be set to zero, which also renders the phase factor $e^{i\xi}$ superfluous. Instead a linear offset was assumed to account for green stray light passing the filter cascade.

The line positions were fixed to the frequencies given in table 4.2. These frequencies were determined using a spectrum at a suitable temperature with all peaks clearly discernible (see Fig. 4.3). As certain peaks are indistinct at higher or lower temperatures, it is appropriate to insert the earlier determined peak positions for all temperatures during the fitting procedure. The dampening constant Γ_ν is constrained to reasonable values in the range of 4 cm^{-1} as a lower limit, representing the bandwidth of the laser system used and 11 cm^{-1} as an upper limit accounting for inhomogeneous line broadening.

The spectra of CaA at low temperatures, starting at room temperature up to 340 K, are dominated by the strong features from the terminal methyl group (r^+, r^+_{FR}). In this temperature region the methylene lines (d^+, d^+_{FR}) appear only as very subtle shoulders in the red wing of the methyl lines. During the process of heating the intensity of the methyl lines decreases significantly, while the methylene ones increase. As expected, no contribution of the terminal methyl group can be detected in the observed spectral region at any temperature, when looking at the deuterated species (see Fig. 4.10 b). In accordance with the non-deuterated spectra the methylene stretching vibrations (d^+, d^+_{FR}) at 2854 and 2924 cm^{-1} are also absent at low temperatures, up to 340 K.

However, a small feature at 2915 cm^{-1} may be discerned in this temperature region in the deuterated case. The origin of this particular line can be attributed to an overtone or combination band of an alkyl chain bending mode that is known to appear in this spectral region [87]. That is also in good agreement with the appearance of the r^+_{FR}-mode at this position in the non-deuterated case. Additionally, a small contribution of the antisymmetric stretching vibration of the methylene group d^- cannot be ruled out [88], although it seems to be unlikely, as the spectra are recorded using the *ssp* polarization combination.

Once the experimental temperature is increased to the range of 360 to 430 K, both

d-lines are observed with increasing strength, in the deuterated and non-deuterated case as well. Similarly, at 470 K the SFG signal drops in both kind of spectra presented in Fig. 4.10 and finally above 470 K no signal from the d^+-line and only a very faint one from the d^+_{FR}-line is discernible from the noise. At temperatures above 510 K the vibrational features in the spectrum are completely lost, which is consistent with the interpretation that the alkyl chains are destroyed by oxidation from ambient air.

From the spectral data presented here in combination with the fit results it is possible to aim at an assessment to which degree gauche defects are present. The approach remains the same as in case of OTS utilizing the ratio $A(d^+)/A(r^+)$.

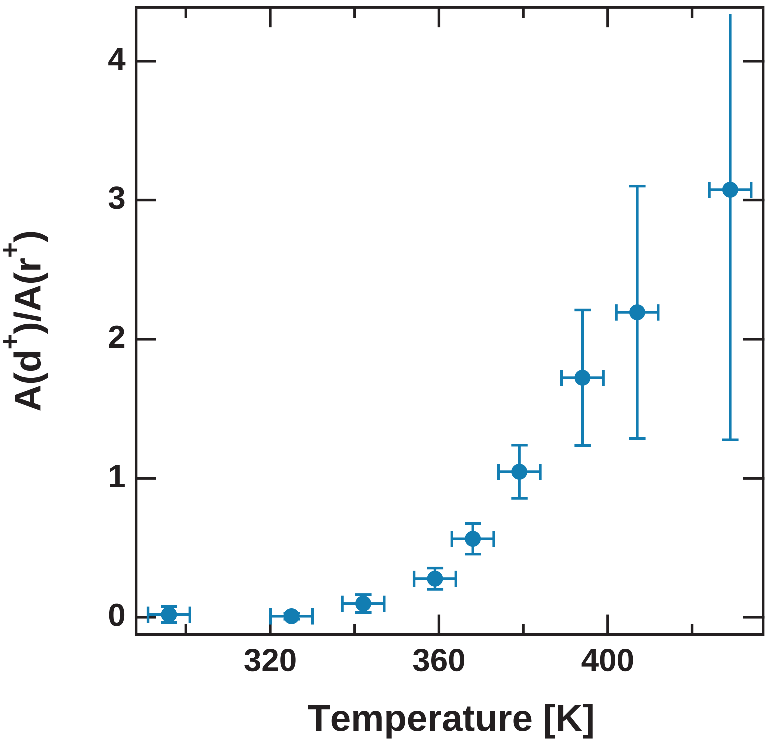

Figure 4.11.: Ratio of the sum-frequency transition strengths of the d^+ and r^+-lines. $A(d^+)/A(r^+)$ determined by fitting the *ssp*-spectra (Fig. 4.10 (a)) at various temperatures. At higher temperatures the error margins are larger due to a smaller SFG signal and therefore a larger uncertainty in the fits to the spectra.

Figure 4.11 shows the ratio of the sum-frequency transition strengths for the d^+ and r^+-lines. As discussed in detail earlier the ratio $A(d^+)/A(r^+)$ is used to discriminate gauche defects from other effects that might influence the SFG signal. As a result the presented ratio can be used to measure the number of gauche defects spatially averaged over the probed surface area.

The ratio found for CaA, in contrast to the data presented for OTS (see Fig. 4.6), is very close to zero at room temperature, due to the near absence of the d^+-mode in the corresponding spectrum (Fig. 4.10 (a)). This suggests that the LB film exhibits a very low density of gauche defects and the molecule's alkyl chains are therefore largely all-*trans* configured, before heating the sample.

The suggestion of a well ordered CaA monolayer is inline with *Outka et al.* [89], who report a high degree of order for CaA on an oxidized Si (111) surface. In their near edge x-ray absorption fine structure (NEXAFS) study they propose layers, where the hydrocarbon chains are estimated to be tilted by 33° [89]. This interpretation is supported by molecular-dynamics (MD) simulations by *Cardini et al.* [90], who also suggest tilted chains with a low defect density.

Yet, different NEXAFS studies by *Kinzler et al.* [33] seem to be in conflict with this interpretation. They have found that CaA monolayers deposited on an oxidized silicon surface exhibit a certain degree of imperfections at room temperature. Still, it is important to note that their study is mainly concerned with the monolayer's structure with respect to molecular tilt angles. Their findings indicate quasi-crystalline domains arranged with tilt angles centered around 30° with respect to the surface normal. But between adjacent domains the tilt angle may point into different azimuthal directions and at the boundaries a quasi-continuous transitions may occur.

As SFG is not sensitive to long-range disorder due to different domains and their boundaries, the chains may still be predominantly all-*trans* configured. While imperfections found by *Kinzler et al.* may well be present, their experiments do not quantify the number of gauche defects in the monolayer. As a result their findings and the data presented here are not in conflict with each other, but rather complementary.

The possibilities and problems related to molecular tilt angle analysis on the basis of SFG data are discussed in a later section.

Further inspection of Fig. 4.11 reveals that the gauche defect density remains at a very low level upon heating, until sample temperatures exceed 340 K. The ratio $A(d^+)/A(r^+)$ increases significantly in the temperature region between 340 and 430 K, indicating a progressive formation of gauche defects.

Assuming an equilibrium constant K, as defined by eq. 4.3, a reaction enthalpy $\Delta_R H$ can be determined using the van't Hoff equation (eq. 4.4).

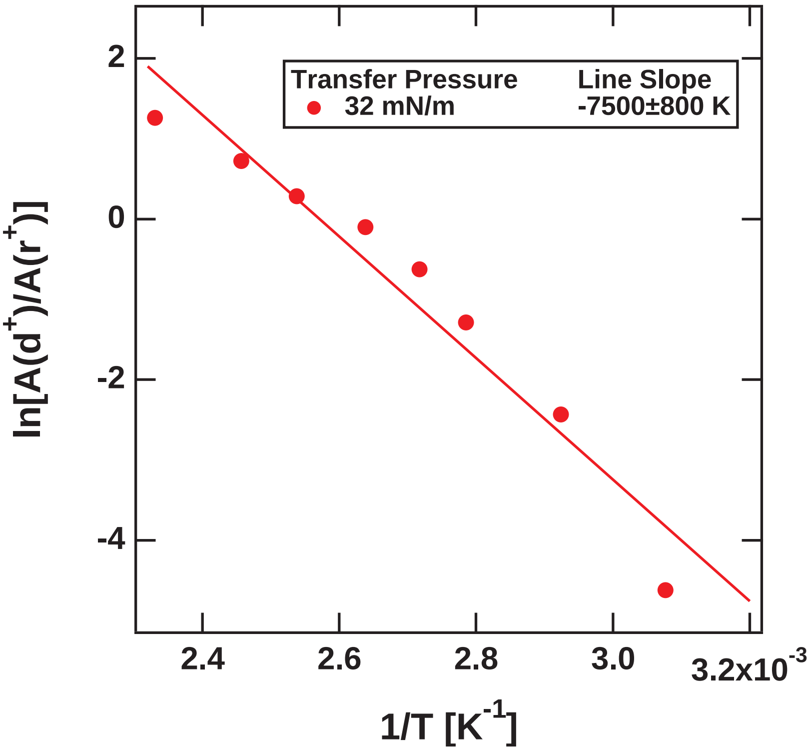

Figure 4.12.: Van't Hoff plot on the basis of the intensity ratio shown in Fig. 4.11.

The van't Hoff plot shown in Fig. 4.12 yields a value of 62 ± 7 kJ/mol for the calculation of $\Delta_R H$. Furthermore, the data presented here can be fitted quite accurately by a straight line. The absence of a kink in the van't Hoff plot supports the assumption that no phase transition occurs in the observed temperature region for the monolayer system. This conclusion is corroborated by temperature dependent NEXAFS data published by *Schertel et al.* [91], who find no evidence for a sharp phase transition in CaA monolayers on $\mathrm{SiO_x}$.

By contrast, multilayer systems of CaA and CdA have been found to show phase transitions in the temperature range from 300 to 400 K [31, 92]. According to *Tippmann-Krayer et al.* a transition from an orthorhombic to a hexagonal lattice can be observed, accompanied by a respective change in area per molecule in the layer [31].

In this context it is interesting to further analyze the packing density in connection to molecular order phenomena. While the packing density in the case of OTS is ultimately governed by the self-assembly process and cannot be microscopically influenced, the different preparation method in case of CaA can be exploited. Here different packing densities may be realized by applying different pressure with the Langmuir trough, whilst maintaining an ordered monolayer on the subphase.

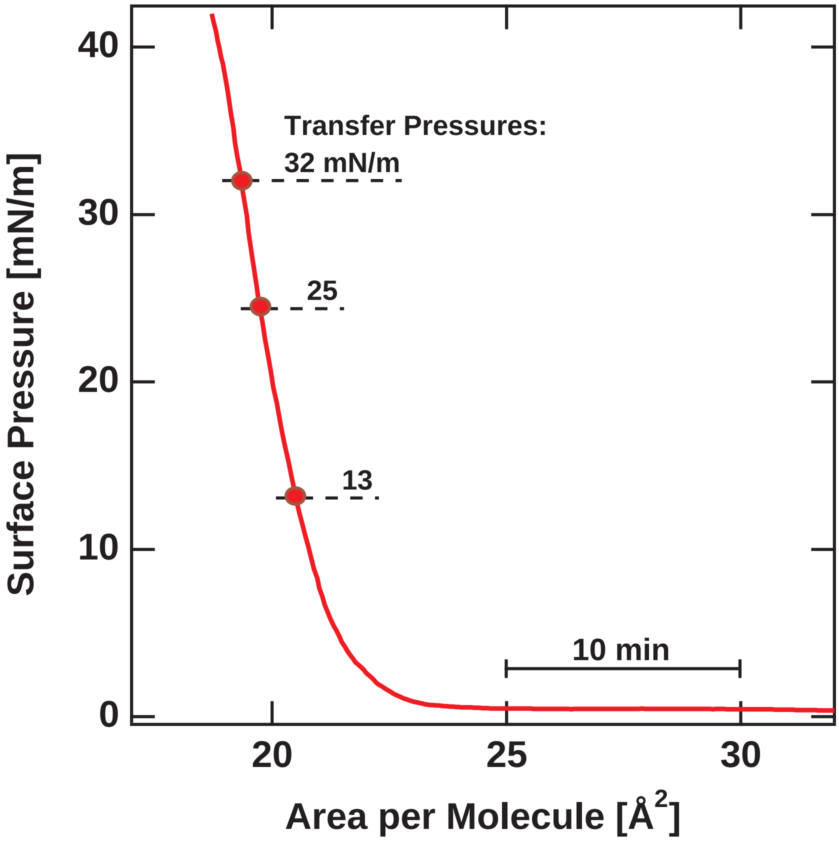

Figure 4.13.: π/A-isotherm of CaA on an aqueous subphase at pH = 8.5 and a Ca^{2+}-concentration of 0.1 mM. The temperature of the subphase is set to 22°C. The typical compression speed is 0.5 Å^2/min. The pressures used for subsequent film transfer are indicated by red dots.

Fig. 4.13 shows a typical π/A-isotherm for the sample system in question. The subphase temperature was held constant at 22 °C for CaA on an aqueous subphase at pH = 8.5. The counter ion concentration for the experiments was set to be 0.1 mM. The compression speed of the barriers was around 0.5 Å^2/min.

While different transfer pressures require the preparation of fresh samples, isotherms of different preparations are sufficiently similar to justify the display of the three transfer pressures used in the context of this thesis in one diagram (red dots in Fig. 4.13).

The data discussed so far correspond to the highest transfer pressure used in this work, 32 mN/m. This transfer pressure was chosen to ensure a well ordered and densely packed monolayer in the so-called *superliquid* (LS) phase [93]. Yet, not near enough to the collapse point of the π/A-isotherm to be at risk of multilayer formation.

Fig. 4.14 may serve to illustrate which lower surface pressures were used for further film transfers.

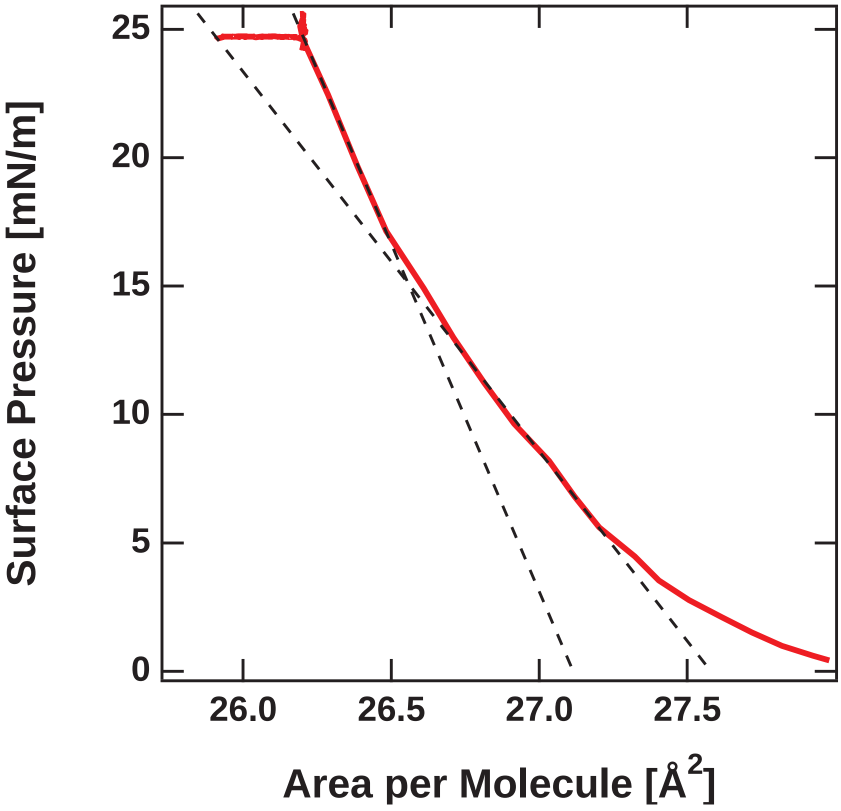

Figure 4.14.: Zoomed in part of an π/A-isotherm of CaA using the same preparation conditions as before. The dashed lines are line fits to indicate parts of the isotherm with different slopes.

The figure shows a zoomed in part of an π/A-isotherm using the same preparation conditions.[2] It is distinct from this isotherm that there is a change in slope around the 15 mN/m pressure mark (see dashed lines in Fig. 4.14). Therefore, this mark was used to identify the presence of the LS phase.

For further experiments it was interesting to see, whether there is a difference just between different transfer pressures (32 and 25 mN/m both in LS phase), between

---

[2] The differing area per molecule is the result of miscalibration and of no importance here.

different phases (LS vs. 13 mN/m as part of the LC phase) or whether the transfer pressure has no influence at all.

In view of the above the same experiments, as discussed for the 32 mN/m case, have been conducted for the variant transfer pressures.

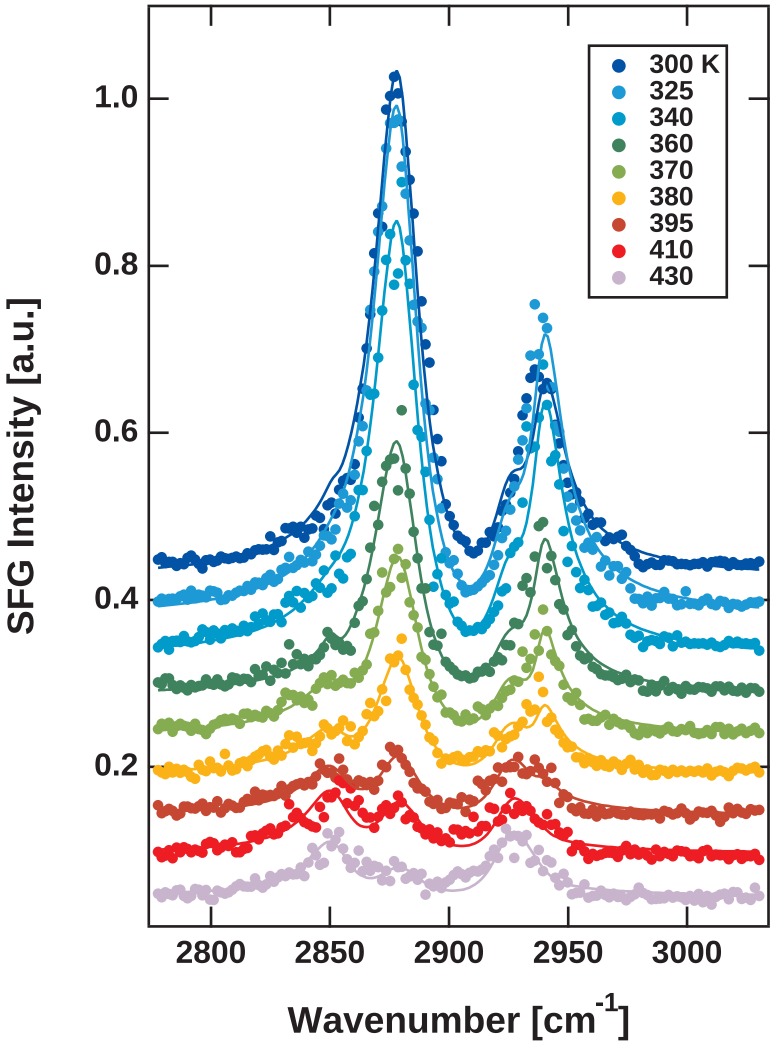

Figure 4.15.: SFG spectra of a glass substrate after deposition of Ca-Arachidate at a transfer pressure of 25 mN/m at various temperatures. All spectra were recorded using *ssp* polarization combination. The solid lines are fits as described in the text. Baselines are separated by a vertical offset.

Figure 4.15 shows the SFG spectra of Ca-Arachidate transferred at a pressure of 25 mN/m, resulting in a monolayer that is still in the LS phase, yet less densely packed when compared to the 32 mN/m case. When compared to the data shown in

Fig. 4.10 it is obvious that the experimental results must be similar, as the evolution of the peaks is almost unchanged.

This is in contrast to the findings in the case of Ca-Arachidate at a transfer pressure of 13 mN/m in the LC phase, shown below (Fig. 4.16).

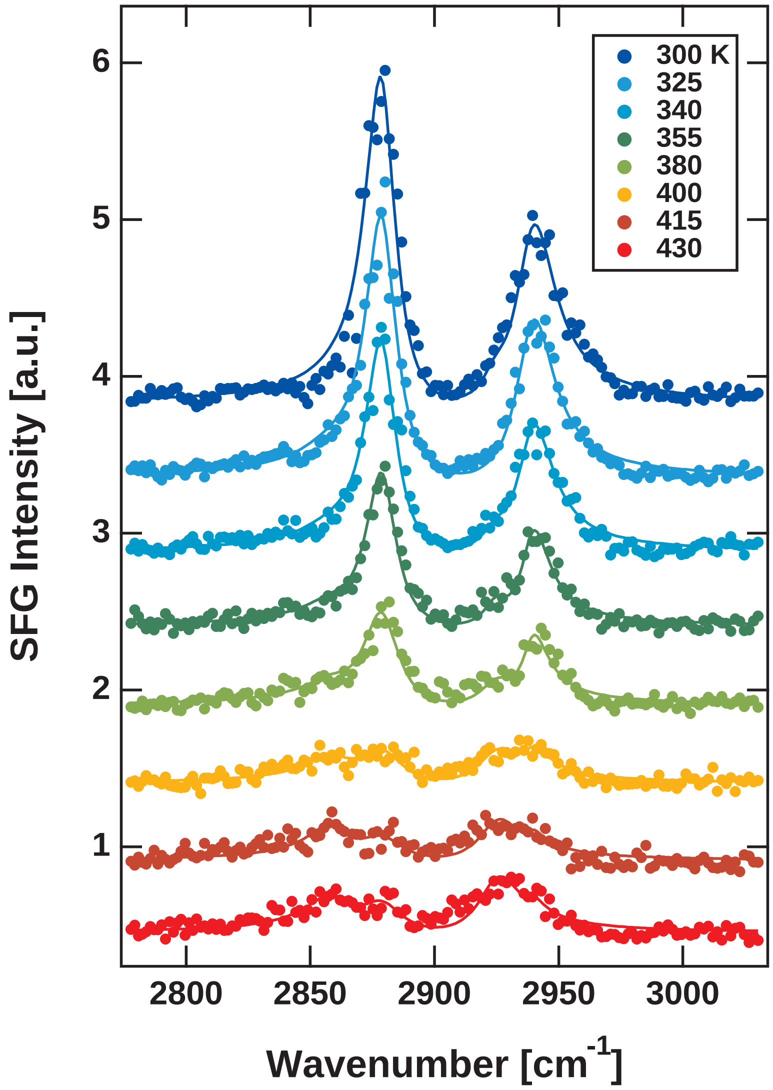

Figure 4.16.: SFG spectra of a glass substrate after deposition of Ca-Arachidate at a transfer pressure of 13 mN/m at various temperatures. All spectra were recorded using *ssp* polarization combination. The solid lines are fits as described in the text. Baselines are separated by a vertical offset.

Here the SFG signal strength is smaller overall and peaks are less pronounced as a result of an inferior S/N ratio. Additionally, signal loss occurs at lower temperatures, when compared to the 25 and 32 mN/m experiments.

It should also be noted that in the fitting process a slightly divergent frequency was found for the d^+-line. Here this line was found to be centered around 2959 cm^{-1} instead of 2954 cm^{-1}. A shift of a few wave numbers is plausible and accounts for slight changes in physical environment perceived by the respective molecular moieties as a result of lower packing density.

On the basis of the resulting data van't Hoff plots for these system can be made.

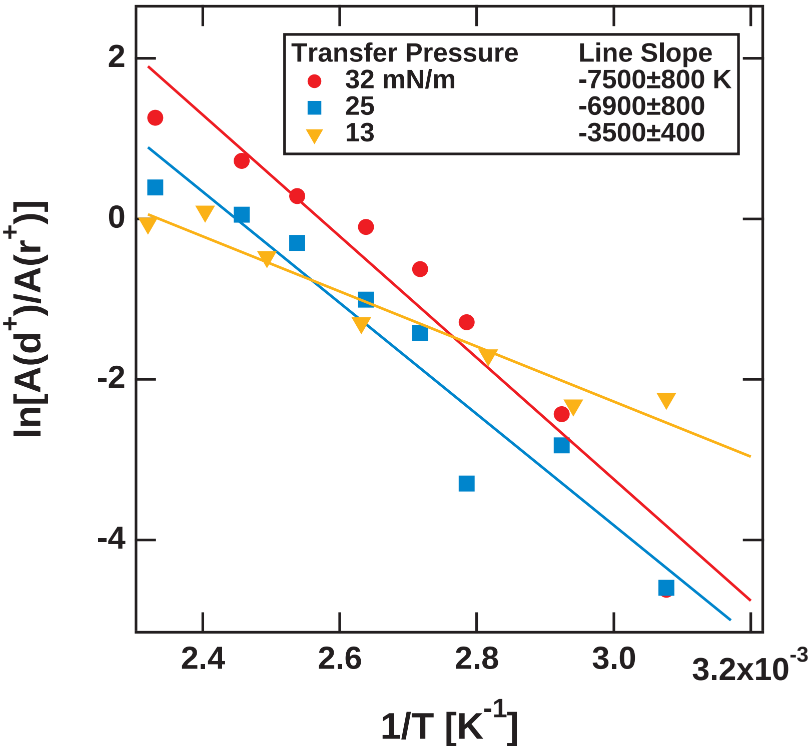

Figure 4.17.: Van't Hoff plots for the different transfer pressure experiments (32 mN/m - red dots, 25 mN/m - blue squares, 13 mN/m - yellow triangles). The solid lines are linear fits to the data. The data for 32 mN/m are the same as in Fig. 4.12 and are presented here for easier comparison.

Fig. 4.17 shows van't Hoff plots based on the results of intensity ratio $A(d^+)/A(r^+)$ comparison for the CaA system at different transfer pressures. The solid lines represent linear fits to the data shown and permit reaction enthalpy $\Delta_R H$ calculation.

For the data shown here reaction enthalpies of 57 ± 7 kJ/mol at 25 mN/m and 29 ± 3 kJ/mol at 13 mN/m can be deduced. These values are close to the 46 kJ/mol [91] found by *Schertel et al.* in their NEXAFS study using a transfer pressure of 25 mN/m [33], reported for CaA on SiO$_x$.

While the calculation of these values seems justified, there is one problem that needs to be addressed in this context. The quantitative relation between the ratio $A(d^+)/A(r^+)$ and the density of gauche defects is not yet fully understood. While the calculation of $\Delta_R H$ on the basis of line slopes in a van't Hoff like manner results in plausible values, the equilibrium constant K does not seem to be equal or directly proportional to the ratio $A(d^+)/A(r^+)$. This becomes apparent when inspecting Fig. 4.17. While the slopes follow the expected trend that a higher compression of the monolayer leads to a higher order and results in a larger $\Delta_R H$, the absolute values of $A(d^+)/A(r^+)$ do not corroborate this idea. In this case it can be expected that the monolayer of lowest packing density have the highest amount of defects, resulting in the largest absolute value of the ratio $A(d^+)/A(r^+)$. As this is not reflected by the data (see. Fig. 4.17), the ratio not solely entails the density of gauche conformers.

These findings suggest that further effects enter into the absolute vales of $A(d^+)/A(r^+)$. Despite this concern it is expedient to assume that the evolution of the ratio $A(d^+)/A(r^+)$ with temperature is reasonable close to the one of gauche defect density. This assumption is backed by the numbers and trend obtained here. In any case the determination of $\Delta_R H$ does not suffer from this problem, since it is extracted from the temperature dependence solely. Any additional factor would only result in an offset in the van't Hoff plot without changing the slope of the line fit, as long as it is not also strongly temperature dependent.

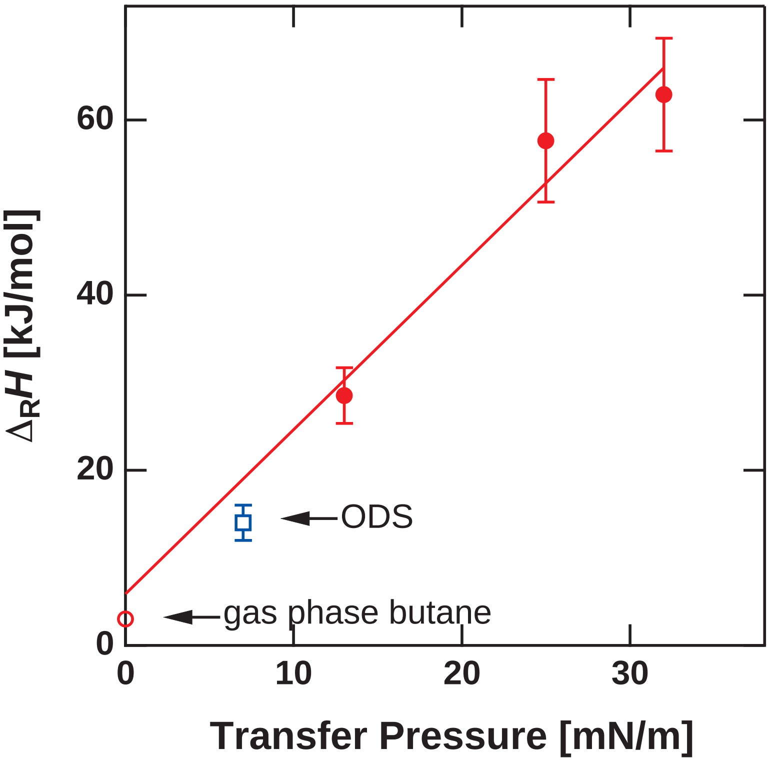

Figure 4.18.: $\Delta_R H$ calculated from the line slopes depicted in Fig. 4.17, plotted versus the transfer pressure. The gas phase value (open red circle) was determined by *Herrebout et al.* [86]. The value for OTS (open blue square) corresponds to the data shown above. The line is an extrapolation of the data and does not include the gas phase and OTS values in the fitting.

Fig. 4.18 depicts the reaction enthalpies obtained at different transfer pressures, as well as the value for gas phase butane, 2.8 kJ/mol [86]. This value may serve as a reference for a theoretical transfer pressure equal to zero, because the gas phase reflects a situation without neighbor interactions.

For further assessment the reaction enthalpy values found for Ca-Arachidate can be brought into connection with the data presented for OTS. As a starting point for this consideration an equivalent of the transfer pressure must be found for an OTS monolayer. The average area per OTS molecule was determined to be about 21 Å^2 [7]. While the intermolecular distance in an OTS monolayer is represented by a mean value of a broader spread due to the lack of long-range order, it is appropriate to assume an hexagonal lattice for the description of an average monolayer.

Based on the hypothetical premiss, that van-der-Waals interactions between the long aliphatic chains are not different, when compared to an LB film, it is possible to correlate the 21 Å^2 area per molecule to a surface pressure of about 7 mN/m, using Fig. 4.13. The resulting pair of values is marked by the open blue square in Fig. 4.18.

While reaction enthalpies found here for the Ca-Arachidate monolayer system are larger, when compared to the respective ones for OTS, they are at least one order of magnitude smaller than the corresponding melting enthalpy of bulk Cd-Arachidate. *Naselli et al.* report a value of about 800 kJ/mol [94] for the melting enthalpy of Cd-Arachidate, a system that is expected to be comparable to the one studied here, as they have an analogous chemical structure.

Still, the results gained in the context of this thesis appear to be in good agreement with other studies in this area. *Marsh* reports a value of 71 kJ/mol [95] for the melting enthalpy of bulk Arachidic acid.

This further supports the premiss, that the approach for the calculation of $\Delta_R H$ as presented here is justified.

4.3. Orientation analysis

When describing an organic monolayer apart from defects within the chain, molecular tilt may be of interest. Vibrational sum-frequency generation spectroscopy represents a tool also suitable for this task. It has been mentioned above, that a SFG signal markedly depends on the light's polarization with respect to molecular orientation for the probed system. The quantitative approach to capitalize on this effect is the so-called *polarization intensity ratio* (PIR) method. While PIR constitutes the historical basis for orientational analysis using SFG, in recent years a refined method, called *polarization null angle* (PNA), has emerged.

A profound analysis on the subject has been published in a review article by *Hong-Fei Wang* and coworkers [63]. Still some basics and their impact on the interpretation of the data presented here will be discussed in this section.

A commonly used entity in the context of orientation analysis employing SFG is the so-called orientational parameter D [63, 96, 97, 98]. D may be defined as follows [96]:

$$D = \frac{\langle cos^3\ \theta \rangle}{\langle cos\ \theta \rangle} = \frac{\chi^{(2)}_{zzz}}{\chi^{(2)}_{zzz} + 2\chi^{(2)}_{zxx}} \tag{4.8}$$

Here the molecular susceptibility tensors $\chi^{(2)}$ are connected to a tilt angle θ, the brackets indicate an expectation value.

While the formalism given in eq. 4.8 appears easy enough at first glance, the described relationship is rather complex. On the one hand this is due to the fact, that the tilt angle θ is not defined consistently. Some publications define θ to be the angle between the molecular long axis and the surface normal, while others relate the tilt of the molecular moiety in question to the surface normal. On the other hand and more importantly the susceptibility tensors, sometimes expressed as effective susceptibilities $\chi^{(2)}_{eff}$, conceal an abundance of experimental quantities. These extend to polarization configuration, incident angle geometry, local field factors in the interface layer, molecular symmetry and hyperpolarizability tensor ratios [63]. It is obvious that for any calculation several assumptions and approximations become necessary.

In case of local field factors typically the problem of finding the correct Fresnel factors has to be simplified. Since the interface layer is molecularly thin and much thiner than the wavelength, it is difficult or impossible to determine the refractive index n_i of this isolated layer. Therefore an approach to deal with this circumstance is to define an effective refractive index n', that may be equal to the one of the bulk phase or based on estimations as summarized by *Shen et al.* [65, 99]. This is done in spite of the fact that the authors state, that the determination of molecular orientation is quite sensitive to the value of n' and using bulk values is not always a good approximation, as the refractive index of the interface layer can be different from that of the bulk material [65].

Additionally it should be noted that refractive indices are wavelength dependent. This problem can be generally simplified by letting $n'(\omega_{SFG}) = n'(\omega_{Vis}) = n'(\omega_{IR})$ in quantitative analysis.

In order to combine hyperpolarizability tensor ratios with symmetry analysis of a molecular vibrational mode the so-called *Raman depolarization ratio and bond polarizability derivative model* is used. In doing so the intensity ratio between the perpendicular component ($I_{(\perp)}$) and the parallel component ($I_{(\|)}$) of Raman scattered light is determined. This ratio, called Raman depolarization ratio (ρ), depends on the symmetry of the molecule and the normal vibrational mode.

$$\rho = \frac{I_{(\perp)}}{I_{(\|)}} \tag{4.9}$$

The experimentally acquired Raman depolarization ratio may then be related to the hyperpolarizability tensor ratio (R) [100, 101]:

$$\rho = \frac{3\gamma^2}{45\alpha^2 + 4\gamma^2} = \frac{3}{4 + 5[(1+2R)/(R-1)]^2} \tag{4.10}$$

Here α and γ are polarizability and anisotropy, respectively [102].

Hyperpolarizability tensor ratios obtained from this model can fairly well quantitatively, if not 100% accurately, reproduce and explain SFG spectra for stretching vibrational modes of the CH_3, CH_2 and CH groups obtained in different polarization configurations [63]. However, to ensure correct R values Raman depolarization measurements for a concrete molecule should be conducted. *Bell et al.*, in this context, have shown, that R, even for the same moiety, may differ. R for the CH_3 group in methanol is found to be 1.7, while it is 3.4 in ethanol [103].

Once these obstacles have been overcome, or satisfyingly approximated, polarization controlled experiments can be done. As mentioned above, molecular symmetry determines the non-zero elements of the molecular polarizability tensor β, that may then be probed by different polarization combinations.

The only major difference remaining is, as mentioned at the outset, the selection of the method. Using the PIR method D is calculated from the polarization intensity ratio of either $\chi^{(2)}_{\mathit{eff,ppp}}/\chi^{(2)}_{\mathit{eff,ssp}}$ or $\chi^{(2)}_{\mathit{eff,sps}}/\chi^{(2)}_{\mathit{eff,ssp}}$ [49, 63, 65]. When recording the respective spectra, the incident angle geometry is preserved.

In the case of the PNA method D is gained by finding a specific polarization set to make the SFG signal become zero (*null*). Here the ratio $\chi^{(2)}_{\mathit{eff,ppp}}/\chi^{(2)}_{\mathit{eff,ssp}}$ is used and incident angles are varied[3] [98, 104].

Therein lies the advantage of PNA over PIR, as the accuracy of a measurement in case of the PNA method is given by the accuracy of arranging the incident angles to find the zero SFG signal angle. This can be done with a precision of about 1 degree, or much less [63]. In contrast, the error margins using the PIR method are defined by the SFG intensities for both polarization combinations probed. This is generally a problem, as peaks strong in one polarization are small in other polarizations [63, 104].

Unfortunately, the optical setup used in the context of this thesis is not equipped to allow PNA method experiments, as incident angles and detection angle cannot be tuned. Therefore results presented subsequently are based on the PIR model.

---

[3] Variation of incident angle also has an influence on the SFG emission angle, that therefore must be adjusted.

Here the signal strength of the symmetric stretching mode (r^+) of the terminal methyl group in the *ssp* and *sps* spectra is used to deduce the tilt angle θ between the molecular symmetry axis of the alkyl chains and the surface normal. Assuming rod like molecules in all-*trans* configuration bound to an azimuthal isotropic surface, the tilt angle can be calculated as described by *Zhang et al.* [105]:

$$\theta = arccot\left[\left(\frac{\chi^{(2)}_{xxz}}{\chi^{(2)}_{xzx}} - \frac{1-R}{1+R}\right)\frac{1-R}{2R}\right]^{\frac{1}{2}} \tag{4.11}$$

A hyperpolarizability tensor ratio R of 2.3 ± 0.3 is used [105]. This value is appropriate, since it results from Raman depolarization studies of a comparable molecule[4].

The nonlinear susceptibilities $\chi^{(2)}_{xxz}$ and $\chi^{(2)}_{xzx}$ can be addressed by applying *ssp* and *sps* polarization combinations, respectively. The resulting ratio can be determined with the fitting procedure based on Eq. 2.11 since $\chi^{(2)}$ is proportional to the resonant contribution of the molecular vibration and therefore proportional to the sum-frequency transition strength A.

Looking at the experimental data presented in Fig. 4.19 it becomes apparent, that the r^+-line cannot be separated from the noise level. This is in good agreement with the fact discussed earlier, that strong peaks in one polarization are small in others. Here, the r^+-line is prominent in the *ssp* polarization combination (see Fig. 4.4) and undiscernible in the case of *sps*. A similar problem has been described by *Shen et al.* [65], where a nearly absent *sps* contribution leads to range of possible orientations of the molecular axis. As a result only an upper limit for molecular tilt angles can be deduced from the data.

Figure 4.20 shows the upper limit of possible molecular tilt angles based on the data presented here, in the temperature range of 300 to 510 K. These findings indicate a molecular tilt not larger than 10° with respect to the surface normal before heating. At room temperature the alkyl chains are standing close to upright on the surface, which is in good agreement with studies of *Ulman*, who reports a tilt angle for OTS SAMs of 0 ± 5° [21]. As temperature increases during heating experiments, the derived tilt angle increases up to a limit of almost 50° until the chain degradation temperature is reached.

---

[4] A long-chain (C_{20}) cyanide was used by *Zhang et al.* [105].

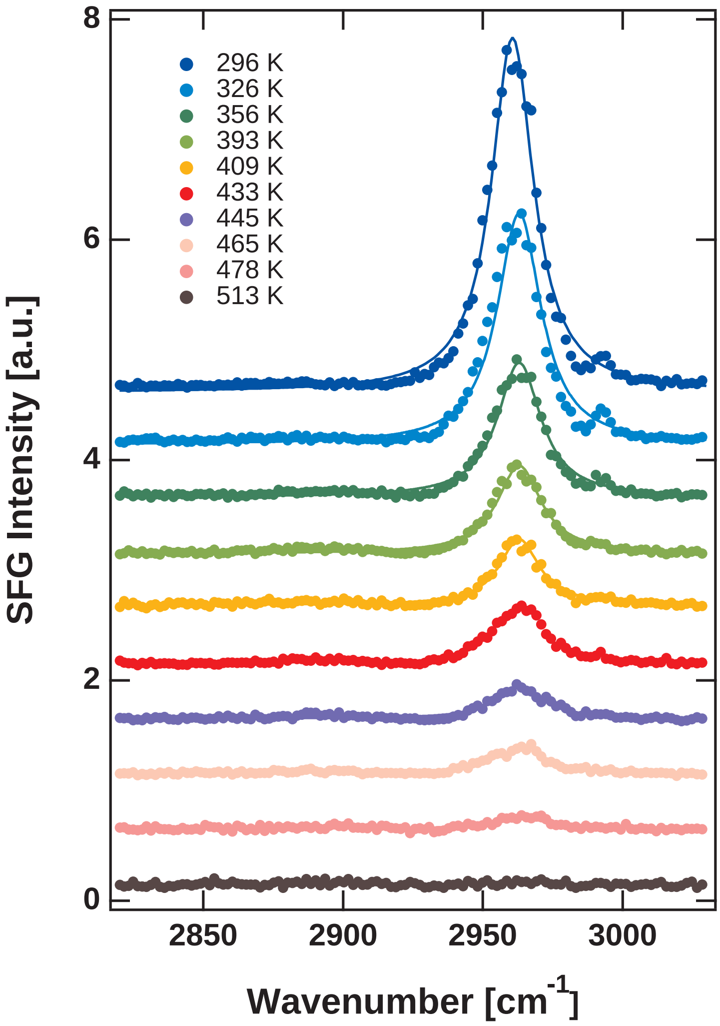

Figure 4.19.: SFG spectra of an OTS covered glass substrate at various temperatures recorded under ambient conditions using *sps* polarization combination. The solid lines are fits using eq. 2.11. The baselines are separated by a vertical offset.

For further comparison it is possible to correlate the tilt angle with the height of an OTS monolayer. In case of an upright all-*trans* conformation the monolayer height is defined by the length of one molecule, resulting in a value of 2.5 nm. Assuming a tilt angle of 50° a reduced height of about 1.6 nm is calculated. The evolution of tilt angles (blue dots) and correlated monolayer height (red triangles) with temperature is depicted in Fig. 4.20. These values allow for comparison with other studies done by *Kim et al.* [77] utilizing AFM to identify the height of an OTS monolayer on SiO_2. They report a monolayer height of 2.5 nm at room temperature and find a reduced height of about 1.5 nm after heating to 550 K [77].

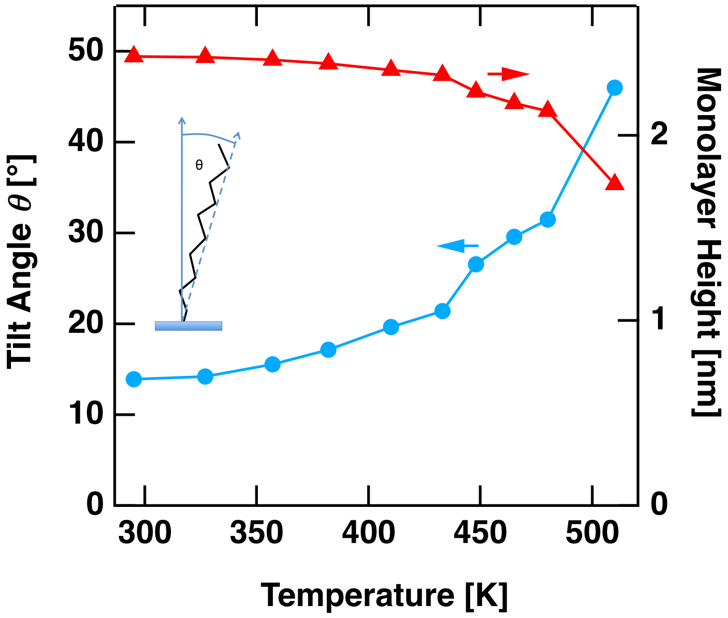

Figure 4.20.: Upper limit for the tilt angle of the molecular symmetry axis of OTS molecules derived from *ssp* and *sps* measurements (blue dots) and calculated height of the monolayer (red triangles).

While calculated tilt angles and monolayer heights derived here are consistent with findings of other groups, as described above, the presented results still have to be interpreted with some caution. On the one hand the afore mentioned assumptions and approximations leave room for deviation and on the other hand any model discussed here assumes a δ-function for the distribution of tilt angles.

While a very narrow dispersion of tilt angles in a densely packed monolayer without defects may be an adequate assumption for some systems, it must surely be called into question in the case of OTS, as studied here. Island growth and pinholes most likely lead to noteworthy amounts of defects and grain boundaries, that would in turn be expected to facilitate a wider distribution of tilt angles.

Unfortunately, the calculation of molecular tilt angles on the basis of SFG suffers from larger uncertainties as the distribution of tilt angles increases. This is due to the fact, that $\chi^{(2)}_{eff}$ is sensitive to a multitude of dependancies and a small fraction of molecules, with one tilt angle, may contribute up to orders of magnitude stronger to the overall SFG signal than a larger fraction with a differing tilt angle.

Disproportional weighting often leads to very similar values for the molecular tilt in praxis. This effect has been found for SHG as well as SFG and is sometimes called *'magic angle'*. In case of SHG the value for the *magic angle* is 39.2° [96] and in the case of SFG it tends towards 60° [106].

As the assumption of a δ-function for the distribution of molecular tilt angles is physically questionable in general and in particular for the system studied here, the significance of the data should not be overrated. Regrettably, this problem is an intrinsic shortcoming of the method and can therefore not be circumvented.

4.4. Conclusions

On the basis of the data presented in this thesis it is now possible to compare the two sample systems discussed earlier. While preparation and binding methods of the two monolayer systems are essentially different, there are rather surprising similarities to be found.

The reaction enthalpies $\Delta_R H$, when regarding the formation of gauche defects with temperature, are comparable. While the numbers are somewhat different, with 14 kJ/mol for OTS and between 29 and 62 kJ/mol for CaA, they are still in the same order of magnitude. A wider span of values for the CaA system is based on the access of different packing densities within the monolayer, by using a Langmuir trough. Yet, performing experiments with varied packing densities of CaA and comparing the results to the findings of OTS leads to mutual trend.

This is especially recognizable when regarding Fig. 4.18, where $\Delta_R H$ is plotted versus the surface pressure. There the presented values for CaA are fitted to a linear regression, that describes the gradient reasonably well. The interesting thing here is now the addition of a *n*-butane gas phase value as well as the OTS value to the plot. While both added values are not part of the regression line calculation, they still fit the presented trend very well. Considering the fact that the additional data describe other systems and in the case of the gas phase value are determined by other groups, using other methods, the similarity between the compared systems is rather astonishing.

The presented results furthermore indicate that neither the chemical nature of the anchor group nor the mobility on the surface play a major rule for the energetics of the formation of gauche defects. Rather, it is likely that the van-der-Waals interaction between the long aliphatic chains dominate the process.

The near linear dependence of $\Delta_R H$ on the surface pressure is also in good agreement with the consideration, that the surface pressure reflects the repulsive forces interacting between the molecules, for a two-dimensional system.

When related to intermolecular distances the observed effect is rather pronounced. In the case of CaA the area per molecule starts at 19.3 Å^2 for a transfer pressure of 32 mN/m and is stepwise increased by first 0.4 Å^2 and then an additional 0.9 Å^2. Assuming a hexagonal lattice the average distance between molecules is varied form 4.4 to 4.6 Å. For this distance change of about 5% the enthalpy changes by a factor of 2.

As a result it seems feasible to regard the intermolecular distance within an organic monolayer, rather then the exact chemical nature, as the governing force behind changes in the energetics of order phenomena.

Against this background, the earlier mentioned energetic similarity between the melting enthalpy of bulk Arachidic acid and the formation of gauche defects in a densely pack monolayer is not surprising. A value of 71 kJ/mol [95] found for the bulk material is close to the reaction enthalpy for the formation of gauche defects within the CaA monolayer, determined to be 62 kJ/mol here.

In concordance with the consideration above, the formation of gauche defects could be interpreted as a form of melting process in common lipids. The CaA monolayer could be seen as analogous to a crystal, an assumption not improbable, when considering the presumed high order and packing density associated with this system.

The observed effect may be described by a so-called *premelting* phenomenon, in which the overall orientational and translational order of the alkyl chains in a monolayer is preserved, whereas single molecules undergo a thermally induced random orientational and conformational disordering process of the chains [107, 108]. In electron diffraction studies *Riegler* has shown, that during the course of premelting the displacements and point imperfections of the headgroup may cause the disordering characteristics. Whereas the main crystal structure remains intact, because the hexagonal diffraction pattern is preserved over the entire temperature range [107]. The described premelting temperature depends on the chain length [107], further supporting the claim that van-der-Waals interactions dominate the monolayer behavior.

The idea of gauche defects forming near the head group, thus far away from the anchor group, is supported by molecular dynamics calculations, done for a similar system [109].

Mar et al. have calculated a percentage of gauche defects as a function of bond number within a long alkyl chain. As a result gauche defects are more likely the higher the sample temperature is and the further the bond in question is away from the anchor group (about 1-5% at 300K and about 12-20% at 425K) [109]. Additionally they predict another feature, namely an alternation of defect concentration within the chain. This feature can be understood by noting that a single gauche defect is unlikely to exist in the middle of the chain because in a densely packed monolayer system, the bend formed by a gauche bond in the middle of the chain would be energetically prohibitive [109].

The following sketches may serve to understand the described effect. Fig. 4.21 shows an arrangement of defect-free molecules, forming a monolayer.

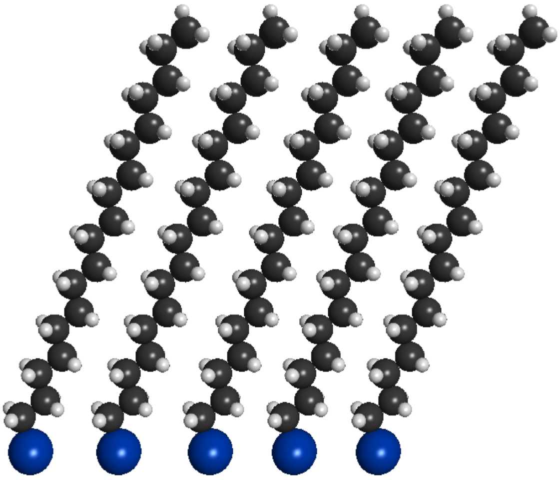

Figure 4.21.: Schematic outline showing a defect-free excerpt of a monolayer.

By contrast Fig. 4.22 shows the same arrangement of molecules, with the addition of a single gauche defect in one chain. It is fairly obvious, that the formation of such a defect must be energetically unfavorable as the required space for the tilted chain is increased. It is intuitive to see, that the nearer to the anchor group the defect is induced, the greater the steric hinderance must be.

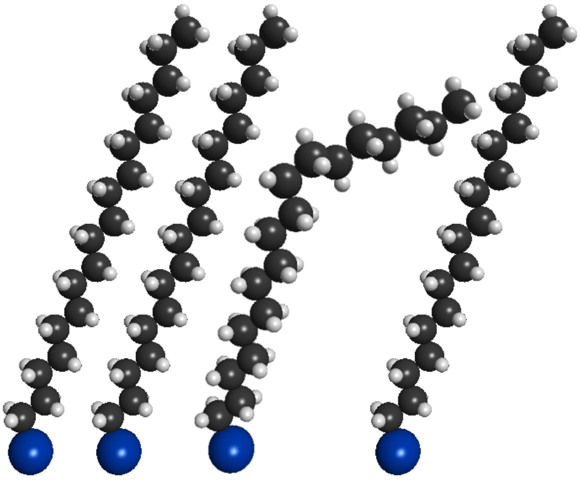

Figure 4.22.: Schematic drawing of a monolayer, one molecule shows a single gauche defect. As a result note the increase in required space.

As a result it is energetically significantly more favorable to form a pair of gauche defects within a single chain as show in Fig. 4.23. Such a pair of defects as depicted is also referred to as a "kink" [109].

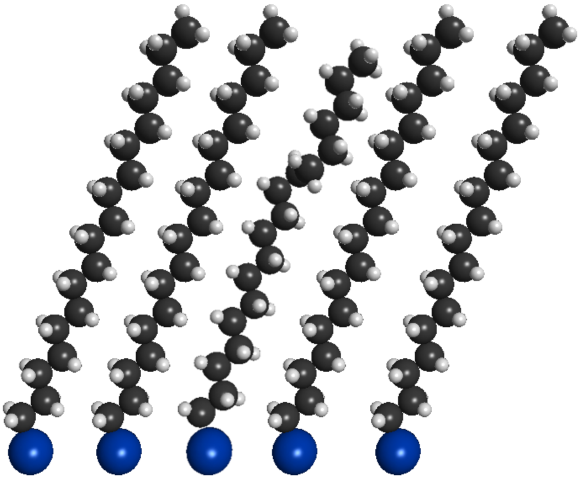

Figure 4.23.: Schematic drawing of a monolayer, one molecule shows a double occurrence of gauche defects. A pair of gauche defects is also referred to as a "kink". Note that the required space is similar to the defect-free case.

An alternation of defect concentration in the chain can be understood on that basis. In this context *Mar et al.* also report a low *gauche* concentration at the first C-C bond (the bond next to the anchor), resulting in a higher defect concentration at odd and a lower concentration at even bond numbers [109].

Additionally these sketches may serve to understand the shortcomings associated with SFG in regard to the presented analysis. While it is obvious that any defect in the chain results in a breaking of the local symmetry, leading to a CH_2 contribution in the SFG signal, the figures also show that there are different situations where the orientation of the terminal CH_3 group is concerned.

A single chain defect certainly results in a change of the head group orientation, most likely resulting in an more anisotropic surface as a consequence of statistical distribution. In that case the r^+-line would be less pronounced in the respective SFG spectrum. Yet, in the case of a kink formation the orientation of the head group is reversed to its original direction, resulting in an unchanged r^+-contribution.

Therein the challenge is founded, when employing SFG spectroscopy as a method to determine absolute values for the number of gauche defects. Here spectroscopy alone is insufficient to solve the problem, as the intensity ratio of the d and r peaks $A(d^+)/A(r^+)$ may be flawed.

The general idea when using this ratio, as described above, is to separate different effects that influence the SFG signal strength. While this approach may work when comparing effects based on the tilt of untwisted alkyl chains vs. isotropy effects, it is incorrect in the context of single *gauche* defects and kinks. In case of a single defect both d and r-contribution are changed, while in the case of a kink defect the d-contribution changes whereas the r-contribution is not altered.

For this reason it is difficult to draw conclusions as to the absolute number of defects within a monolayer, only based on spectroscopical data.

Consulting molecular dynamics (MD) simulations, the probability for finding a gauche conformation per C-C bond is found to be around 4% at 300 K and between 10 and 20% at 425 K for alkylthiols on gold at an area per molecule of 21.6 Å^2 [109]. As the layers studied here are more tightly packed, slightly smaller values are to be expected. In the context of area dependency in LB layers *Karaborni et al.* have shown that at 18.5 and 19 Å^2/molecule the probability that the monolayer is completely *trans* at any time is about 92%, but decreases to about 77% at 20 Å^2, using MD simulations [110].

In order to obtain a value for K in line with the MD modeling, e.g. 5%, a proportionality factor c of about 250 is necessary, when compared with the spectroscopically gained data through $A(d^+)/A(r^+)$. Such a factor may be explained by the fact that there are 17 different sites for a gauche defect in a C_{20} chain molecule. This idea goes along with high values of $\Delta_R S$, which are estimated to be in the range of 100 J/mol K for long aliphatic chains [85].

Still, the determination of a value for the Gibb's free energy $\Delta_R G$ remains vague due to the unsettled nature of the factor c. As gauche defects are spectroscopically verifiable even at quite low temperatures, $\Delta_R G$ has to be fairly low. Even though employing a Boltzmann distribution on the basis of the $\Delta_R G \approx 5$ kJ/mol calculated for OTS in chapter 4.2.1, results in every second bond being in the *gauche* conformation.

This result clearly contradicts other studies including MD modeling in this area and is most likely flawed due to the as of yet certainly not completely understood relation between $A(d^+)/A(r^+)$ and K.

Unfortunately, the data presented here do not allow for calculation of an activation energy in an Arrhenius like manner since there is no time resolution and therefore no rate constant k for the reaction accessible.

However, the analysis of $\Delta_R H$ does not suffer from this problem, though it should be noted that its value is likely an average over many different microscopic configurations.

4.5. Outlook

While the experiments performed in the context of this thesis show, that SFG spectroscopy is a powerful tool to gain insight into the behavior of organic monolayers, there is also room for further improvements.

Two starting points for improvement approaches are promising.

On the one hand the preparational side may be varied. Here advanced experiments could be introduced using deviant surrounding gases. Repeating the work shown here, utilizing an inert gas such as argon or nitrogen or a reactive candidate such as pure oxygen, could help in the assessment of the matrix influence. Possible changes are expected to influence the stability of the organic monolayer is question, especially with respect to the reversibility of gauche defect formation.

On the other hand, and probably more importantly, the analytical side could be improved. Here advanced modeling and molecular dynamics calculations could be compared to simulations of SFG spectra. In order for this approach to work it would be essential to eliminate some of the uncertainties afflicting the SFG spectra at the moment.

Primarily it would be beneficial to use the *polarization null angle* method as a superior form of orientational analysis. Paired with theoretical works it might be possible to distinguish spectroscopical features originating from whole chain tilt events and defect formation.

5. Summary

Organic monolayers have been an area of interest for decades in the field of surface science. Due to the evolution of analytical methods alongside engineering potential, this interest has been renewed and extended in the last years. Organic monolayers are of special interest as they have the potential to bridge the gap between inorganic substrates and biological material as well as their potential for specific surface modification. This potential is mainly founded in the ability to tailor surfaces in the desired form and function alike by modification of organic layer.

Modern methods have shown that structuring [13], functionalization [111] and even switching of individual properties [1] is possible with fitting candidates of these organic monolayers.

In the context of this thesis, studies on the orientational and conformational properties of different organic monolayers have successfully been performed. It is comprehensible that the orientation and conformation within the monolayer defines the overall order and may well have an influence on any technical step to modify certain characteristics. Therefore, OTS has been chosen as an example for a self-assembled monolayer that is covalently bound to the substate. CaA is employed as a candidate for a monolayer coated to the substrate by the *Langmuir-Blodgett* technique.

Both molecules constituting the respective monolayers have been described as well ordered before, using X-ray grazing incidence diffraction or atomic force microscopy [20, 35]. Yet, most of the analytical methods used in the past suffer from shortcomings with regard to reflecting realistic conditions for the everyday use of tailored monolayers. Ambient conditions as well as temperatures above room temperature are expected to have an influence on the organic monolayer and while very common in engineering, are underrepresented in analytical science.

Here vibrational sum-frequency generation spectroscopy has been used, since this method is noninvasive as well as intrinsically surface sensitive, due to the unique selection rules, even when used in air. For analysis the separate monolayers have in each case been attached to a glass substrate to minimize heating effects by the used green laser beam. It was then possible to heat the whole sample in a well controlled manner by classical resistance heating.

Illuminating the organic monolayer on top simultaneously with a pulsed green and infrared laser beam results in sum-frequency generation, containing vibrational information on specific molecular moieties at the surface. Vibrational spectra gained this way could be evaluated and certain modes identified.

Both molecules sampled have long aliphatic chains and both methyl- and methylene-groups can be identified in the SFG spectra. The frequency, in the *ssp* polarization combination, associated with the symmetric stretch of the terminal -CH_3 group was found to be 2878 cm^{-1}, the symmetric stretch of the chains $=CH_2$ groups could be detected at 2854 cm^{-1} and the respective Fermi resonances were located at 2938 and 2924 cm^{-1}.

Repetitive execution of spectroscopical experiments, while changing the sample temperature, leads to diverse responses for the described lines. Performing a deconvolution analysis by fitting the spectra to a function for the overall SFG intensity results in values for transition strength of unique modes.

On the basis of that data it is possible to quantify these results, in the form of a calculation for the reaction enthalpy $\Delta_R H$ of an *anti/gauche*-transition. Additional information could be gained by comparing the enthalpy values found this way with the respective transfer pressure, as a description for intermolecular forces.

Table 5.1.: $\Delta_R H$ of an *anti/gauche*-transition for the different systems analyzed.

System	$\Delta_R H$ **[kJ/mol]**
OTS	14
CaA (13mN/m)	29
CaA (25mN/m)	57
CaA (32mN/m)	62

By consulting another polarization combination (*sps*), it is even possible to assess an upper limit of molecular tilt angle for the long chains. On the basis of the data presented here, the chains are tilted by about 10° at room temperature which increases up to nearly 50°, with respect to the surface normal, under the influence of heating.

While it has to be noted that some modeling is necessary and assumptions need to be made, the results presented here still help in the understanding of ordering phenomena in organic monolayers on a molecular level.

It could be shown, that SFG is an appropriate method for the analysis, as the results presented here are in good agreement with other studies in the literature, while contributing valuable new insights, especially with respect to higher temperatures. The presented values for the reaction enthalpy of *gauche*-defect formation (see Tab. 5) are inaccessible by other methods and help in the understanding of the microscopical picture of an organic monolayer.

The main aspects regarding the monolayer structure proven by this thesis are:

- The formation of conformational changes seems to primarily depend on van-der-Waals interactions between the chains and accordingly the intermolecular distance. This is in contrast to considerations that anchor groups to the surface or preparation method could be the dominating influence. This assumption is in agreement with the common trend in the development of $\Delta_R H$ for different systems with respect to the transfer pressure (see Fig. 4.18).
- The low enthalpy values for the formation of *gauche*-defects, as well as the non-zero contribution of the d^+-line in SFG spectra strongly suggest an easy formation of conformational changes within the monolayer. The typical picture of a very well ordered monolayer, especially of lower packing density or at higher temperature, seems to be inappropriate.

These findings should be taken into account, when for example considering the modification of chain end groups by click chemistry in order to tune the monolayer attributes. Higher temperatures in such an approach could lead to buried end groups, due to induced disorder by conformational changes. Here passivation and less efficient modification could be the consequence.

Bibliography

[1] C. Amiri Naini, S. Franzka, S. Frost, M. Ulbricht, and N. Hartmann, Angewandte Chemie International Edition **50**, 4513 (2011).

[2] A. Pockels, Nature **43**, 437 (1891).

[3] I. Langmuir, Journal of the American Chemical Society **39**, 1848 (1917).

[4] I. Langmuir, Trans. Faraday Soc. **15**, 62 (1920).

[5] K. B. Blodgett, Journal of the American Chemical Society **57**, 1007 (1935).

[6] K. B. Blodgett and I. Langmuir, Physical Review **51**, 964 (1937).

[7] F. Schreiber, Progress in Surface Science **65**, 151 (2000).

[8] R. Singhvi, A. Kumar, G. P. Lopez, G. N. Stephanopoulos, D. Wang, G. M. Whitesides, and D. E. Ingber, Science **264**, 696 (1994).

[9] C. B. Gorman, H. A. Biebuyck, and G. M. Whitesides, Chemistry of Materials **7**, 526 (1995).

[10] W. S. Beh, I. T. Kim, D. Qin, Y. Xia, and G. M. Whitesides, Advanced Materials **11**, 1038 (1999).

[11] J. D. Cox, M. S. Curry, S. K. Skirboll, P. L. Gourley, and D. Y. Sasaki, Biomaterials **23**, 929 (2002).

[12] P. Silberzan, L. Leger, D. Ausserre, and J. Benattar, Langmuir **7**, 1647 (1991).

[13] T. Balgar, *Laserstrukturierung von Alkylsiloxanmonoschichten auf Siliziumsubstraten im Submikrometerbereich*, Ph.D. thesis, Universität Duisburg-Essen (2005).

[14] C. Carraro, O. W. Yauw, M. M. Sung, and R. Maboudian, The Journal of Physical Chemistry B **102**, 4441 (1998).

[15] C. Tripp and M. Hair, Langmuir **8**, 1120 (1992).

[16] A. Richter, M. Durbin, C.-J. Yu, and P. Dutta, Langmuir **14**, 5980 (1998).

[17] R. Bautista, N. Hartmann, and E. Hasselbrink, Langmuir **19**, 6590 (2003).

[18] Y. Wang and M. Lieberman, Langmuir **19**, 1159 (2003).

[19] A. Glaser, J. Foisner, H. Hoffmann, and G. Friedbacher, Langmuir **20**, 5599 (2004).

[20] I. Tidswell, T. Rabedeau, P. S. Pershan, S. Kosowsky, J. Folkers, and G. M. Whitesides, The Journal of Chemical Physics **95**, 2854 (1991).

[21] A. Ulman, Chemical Reviews **96**, 1533 (1996).

[22] T. Nakagawa, K. Ogawa, and T. Kurumizawa, Langmuir **10**, 525 (1994).

[23] D. L. Allara, A. N. Parikh, and F. Rondelez, Langmuir **11**, 2357 (1995).

[24] J. Rühe, V. Novotny, K. Kanazawa, T. Clarke, and G. Street, Langmuir **9**, 2383 (1993).

[25] B. Bhushan, A. V. Kulkarni, V. N. Koinkar, M. Boehm, L. Odoni, C. Martelet, and M. Belin, Langmuir **11**, 3189 (1995).

[26] S. R. Wasserman, Y. T. Tao, and G. M. Whitesides, Langmuir **5**, 1074 (1989).

[27] S. R. Cohen, R. Naaman, and J. Sagiv, The Journal of Physical Chemistry **90**, 3054 (1986).

[28] M. Calistri-Yeh, E. J. Kramer, R. Sharma, W. Zhao, M. Rafailovich, J. Sokolov, and J. Brock, Langmuir **12**, 2747 (1996).

[29] D. J. Ahn and E. I. Franses, The Journal of Chemical Physics **95**, 8486 (1991).

[30] V. Fainerman, D. Vollhardt, and R. Johann, Langmuir **16**, 7731 (2000).

[31] P. Tippmann-Krayer, R. Kenn, and H. Möhwald, Thin Solid Films **210**, 577 (1992).

[32] D. Outka, J. Stöhr, J. Rabe, J. Swalen, and H. Rotermund, Physical Review Letters **59**, 1321 (1987).

[33] M. Kinzler, A. Schertel, G. Hähner, C. Wöll, M. Grunze, H. Albrecht, G. Holzhüter, and T. Gerber, The Journal of Chemical Physics **100**, 7722 (1994).

[34] G. Cardini, J. P. Bareman, and M. L. Klein, Chemical Physics Letters **145**, 493 (1988).

[35] D. Y. Takamoto, E. Aydil, J. A. Zasadzinski, A. T. Ivanova, D. K. Schwartz, T. Yang, and P. S. Cremer, Science **293**, 1292 (2001).

[36] R. Herrmann, C. Onkelinx, et al., Pure and Applied Chemistry **58**, 1737 (1986).

[37] N. B. Colthup, L. H. Daly, and S. E. Wiberley, *Introduction to infrared and Raman spectroscopy* (Academic press, 1990).

[38] M. Baia, S. Astilean, and T. Iliescu, *Raman and SERS investigations of pharmaceuticals* (Springer, 2008).

[39] X. Zhu, H. Suhr, and Y. Shen, Phys. Rev. B: Condens. Matter;(United States) **35** (1987).

[40] P. J. Mohr, B. N. Taylor, and D. B. Newell, Rev. Mod. Phys. **80**, 633 (2008).

[41] M. Buck and M. Himmelhaus, Journal of Vacuum Science & Technology A: Vacuum, Surfaces, and Films **19**, 2717 (2001).

[42] F. Vidal and A. Tadjeddine, Reports on Progress in Physics **68**, 1095 (2005).

[43] G. Mahan and A. Lucas, The Journal of Chemical Physics **68**, 1344 (1978).

[44] B. Persson and R. Ryberg, Physical Review B **24**, 6954 (1981).

[45] R. S. Sorbello, Physical Review B **32**, 6294 (1985).

[46] M. W. Severson, C. Stuhlmann, I. Villegas, and M. J. Weaver, The Journal of chemical physics **103**, 9832 (1995).

[47] P. Jakob, The Journal of Chemical Physics **114**, 3692 (2001).

[48] M. Cho, C. Hess, and M. Bonn, Physical Review B **65**, 205423 (2002).

[49] P. Guyot-Sionnest, J. Hunt, and Y. Shen, Physical Review Letters **59**, 1597 (1987).

[50] S. Roke, J. Schins, M. Muller, and M. Bonn, Physical Review Letters **90**, 128101 (2003).

[51] P. F. Bernath, *Spectra of atoms and molecules* (Oxford University Press, 2005).

[52] N. Akamatsu, K. Domen, and C. Hirose, The Journal of Physical Chemistry **97**, 10070 (1993).

[53] Y. Shen, Annual Review of Physical Chemistry **40**, 327 (1989).

[54] F. Eisert, O. Dannenberger, and M. Buck, Physical Review B **58**, 10860 (1998).

[55] E. H. Backus, N. Garcia-Araez, M. Bonn, and H. J. Bakker, The Journal of Physical Chemistry C **116**, 23351 (2012).

[56] A. Ulman, *An introduction to ultrathin organic films: From Langmuir-Blodgett to self-assembly* (Academic Press: Boston, 1991).

[57] V. M. Kaganer, H. Möhwald, and P. Dutta, Reviews of Modern Physics **71**, 779 (1999).

[58] H.-J. Butt, K. Graf, and M. Kappl, *Physics and chemistry of interfaces* (Wiley-VCH, Verlag GmbH & Co., KGaA, Weinheim, Germany, 2006).

[59] K. Laß, *Zur Schwingungs- und Photodesorptionsdynamik von Kohlenstoffmonoxid auf einer Silizium(100)-Oberfläche*, Ph.D. thesis, Universität Duisburg-Essen (2008).

[60] N. Ji, V. Ostroverkhov, C.-Y. Chen, and Y.-R. Shen, Journal of the American Chemical Society **129**, 10056 (2007).

[61] S. Nihonyanagi, A. Eftekhari-Bafrooei, and E. Borguet, The Journal of Chemical Physics **134**, 084701 (2011).

[62] B. Chow, T. Ehler, and T. Furtak, Applied Physics B **74**, 395 (2002).

[63] H.-F. Wang, W. Gan, R. Lu, Y. Rao, and B.-H. Wu, International Reviews in Physical Chemistry **24**, 191 (2005).

[64] C. D. Bain, P. B. Davies, T. H. Ong, R. N. Ward, and M. A. Brown, Langmuir **7**, 1563 (1991).

[65] X. Zhuang, P. Miranda, D. Kim, and Y. Shen, Physical Review B **59**, 12632 (1999).

[66] Y. Liu, L. K. Wolf, and M. C. Messmer, Langmuir **17**, 4329 (2001).

[67] Y. Tong, E. Tyrode, M. Osawa, N. Yoshida, T. Watanabe, A. Nakajima, and S. Ye, Langmuir **27**, 5420 (2011).

[68] J. Löbau, A. Rumphorst, K. Galla, S. Seeger, and K. Wolfrum, Thin Solid Films **289**, 272 (1996).

[69] S. Ye, S. Nihonyanagi, and K. Uosaki, Physical Chemistry Chemical Physics **3**, 3463 (2001).

[70] J. Holman, P. B. Davies, T. Nishida, S. Ye, and D. J. Neivandt, The Journal of Physical Chemistry B **109**, 18723 (2005).

[71] S. Ye, H. Noda, T. Nishida, S. Morita, and M. Osawa, Langmuir **20**, 357 (2004).

[72] J. Rabe, J. Rabolt, C. Brown, and J. Swalen, The Journal of Chemical Physics **84**, 4096 (1986).

[73] R. MacPhail, H. Strauss, R. Snyder, and C. Elliger, The Journal of Physical Chemistry **88**, 334 (1984).

[74] J. R. Chamberlain and J. E. Pemberton, Langmuir **13**, 3074 (1997).

[75] I. Safarik and O. P. Strausz, Research on Chemical Intermediates **22**, 275 (1996).

[76] G. J. Kluth, M. M. Sung, and R. Maboudian, Langmuir **13**, 3775 (1997).

[77] H. K. Kim, J. P. Lee, C. R. Park, H. T. Kwak, and M. Sung, The Journal of Physical Chemistry B **107**, 4348 (2003).

[78] R. Snyder, H. Strauss, and C. Elliger, The Journal of Physical Chemistry **86**, 5145 (1982).

[79] M. R. Watry, T. L. Tarbuck, and G. L. Richmond, The Journal of Physical Chemistry B **107**, 512 (2003).

[80] T. Balgar, R. Bautista, N. Hartmann, and E. Hasselbrink, Surface Science **532**, 963 (2003).

[81] D. K. Schwartz, Annual Review of Physical Chemistry **52**, 107 (2001).

[82] Y.-a. Cheng, B. Zheng, P.-h. Chuang, and S. Hsieh, Langmuir **26**, 8256 (2010).

[83] T. Koga, K. Honda, S. Sasaki, O. Sakata, and A. Takahara, Langmuir **23**, 8861 (2007).

[84] M. C. Gurau, E. T. Castellana, F. Albertorio, S. Kataoka, S.-M. Lim, R. D. Yang, and P. S. Cremer, Journal of the American Chemical Society **125**, 11166 (2003).

[85] T. Heimburg, *Thermal biophysics of membranes* (Wiley-VCH, 2007).

[86] W. Herrebout, B. Van der Veken, A. Wang, and J. Durig, The Journal of Physical Chemistry **99**, 578 (1995).

[87] G. Herzberg, *Molecular Spectra and Molecular Structure, II. Infrared and Raman Spectra of Polyatomic Molecules* (Krieger Publishing Company, 1991).

[88] R. N. Ward, D. C. Duffy, P. B. Davies, and C. D. Bain, The Journal of Physical Chemistry **98**, 8536 (1994).

[89] D. Outka, J. Stöhr, J. Rabe, and J. Swalen, The Journal of Chemical Physics **88**, 4076 (1988).

[90] J. P. Bareman, G. Cardini, and M. L. Klein, Physical Review Letters **60**, 2152 (1988).

[91] A. Schertel, G. Hähner, M. Grunze, and C. Wöll, Journal of Vacuum Science & Technology A **14**, 1801 (1996).

[92] A. Gupta, P. Rajput, S. Bernstorff, and H. Amenitsch, Langmuir **24**, 7793 (2008).

[93] M. Kurnaz and D. Schwartz, The Journal of Physical Chemistry **100**, 11113 (1996).

[94] C. Naselli, J. Rabolt, and J. Swalen, The Journal of Chemical Physics **82**, 2136 (1985).

[95] D. Marsh, *Handbook of lipid bilayers* (CRC Press, 2013).

[96] G. J. Simpson and K. L. Rowlen, Journal of the American Chemical Society **121**, 2635 (1999).

[97] G. J. Simpson, S. G. Westerbuhr, and K. L. Rowlen, Analytical Chemistry **72**, 887 (2000).

[98] Y. Rao, Y.-s. Tao, and H.-f. Wang, Journal of Chemical Physics **119**, 5226 (2003).

[99] X. Wei, S.-C. Hong, X. Zhuang, T. Goto, and Y. Shen, Physical Review E **62**, 5160 (2000).

[100] M. Colles and J. Griffiths, The Journal of Chemical Physics **56**, 3384 (1972).

[101] C. Hirose, N. Akamatsu, and K. Domen, Applied Spectroscopy **46**, 1051 (1992).

[102] D. Long, Proceedings of the Royal Society of London. Series A. Mathematical and Physical Sciences **217**, 203 (1953).

[103] G. Bell, Z. Li, C. Bain, P. Fischer, and D. Duffy, The Journal of Physical Chemistry B **102**, 9461 (1998).

[104] R. Lu, W. Gan, B.-h. Wu, H. Chen, and H.-f. Wang, The Journal of Physical Chemistry B **108**, 7297 (2004).

[105] D. Zhang, J. Gutow, and K. Eisenthal, The Journal of Physical Chemistry **98**, 13729 (1994).

[106] K. Cimatu and S. Baldelli, The Journal of Physical Chemistry C **111**, 7137 (2007).

[107] J. E. Riegler, The Journal of Physical Chemistry **93**, 6475 (1989).

[108] S. D. Evans, R. Sharma, and A. Ulman, Langmuir **7**, 156 (1991).

[109] W. Mar and M. L. Klein, Langmuir **10**, 188 (1994).

[110] S. Karaborni and S. Toxvaerd, The Journal of Chemical Physics **96**, 5505 (1992).

[111] B. Klingebiel, A. Schröter, S. Franzka, and N. Hartmann, ChemPhysChem **10**, 2000 (2009).

A. Appendix

A.1. List of abbreviations

Table A.1.: Abbreviations and symbols used

Symbol	**Meaning**
A	IR & Raman transition dipole moment
α	Raman transition dipole moment
α_e	electronic polarizability
α_ν	vibrational polarizability
β	hyperpolarizability
χ	susceptibility
χ, θ, ϕ	*Euler angles*
ϵ_0	vacuum electric constant
$\vec{E}$	electric field
γ	surface tension
Γ	bandwidth
I	intensity
λ	wavelength
μ	IR transition dipole moment
N	number of SFG active molecules
ω	frequency
π	surface pressure
Θ	fractional coverage
$\vec{P}$	polarization
R	hyperpolarizability tensor ratio
$\tilde{U}$	dipole sum
ξ	phase factor
AFM	atomic force microscopy

continued on next page

Table A.1 – *continued from previous page*

Symbol	**Meaning**
CaA	calcium arachidate
BBO	beta barium borate
DFG	difference frequency generation
FWHM	full width at half maximum
GIXD	grazing incident X-ray diffraction
IR	infrared
LB	Langmuir-Blodgett
L_1, LE	liquid-expanded phase
L_2, LC	liquid-condensed phase
LS	superliquid phase
MD	molecular-dynamics
NEXAFS	near edge X-ray absorption fine structure
Nd:YAG	neodymium-doped yttrium aluminium garnet
OPA	optical parametric amplifier
OPG	optical parametric generator
OPO	optical parametric oscillator
OTS	octadecyltrichlorosilane
PIR	polarization intensity ratio
PMT	photomultiplier tube
PNA	polarization null angle
PNiPAAm	poly(N-isopropylacrylamide)
S	solid phase
S/N	signal-to-noise ratio
SAM	self-assembled monolayer
SERS	surface-enhanced Raman scattering
SFG	sum-frequency generation
SHG	second harmonic generation
t	time
vis	visible

A.2. Fit results

The following tables show the fit results used for further calculations done in this thesis. For easier comparison the results are normalized against the strongest peak contribution for each experiment, which is set to 1.

Table A.2.: Fit results for the OTS system.

T [K]	$A(d^+)$ [a.u.]	$A(r^+)$ [a.u.]
295	0.184377	1
327	0.216058	0.95816
357	0.282739	0.800689
382	0.399103	0.659239
410	0.479662	0.503924
433	0.489267	0.424618
448	0.598318	0.277977
465	0.612119	0.224689
480	0.596916	0.199345
510	0.567548	0.0971694

Table A.3.: Fit results for the CaA (13 mN/m) system.

T [K]	$A(d^+)$ [a.u.]	$A(r^+)$ [a.u.]
296	0.00414562	1
325	0.0966773	0.905374
340	0.0791332	0.805596
355	0.122932	0.671396
380	0.162487	0.594424
401	0.250823	0.402148
416	0.33943	0.308524
431	0.339266	0.358615

Table A.4.: Fit results for the CaA (25 mN/m) system.

T [K]	$A(d^+)$ [a.u.]	$A(r^+)$ [a.u.]
296	0.0108637	1
325	0.0100505	0.993847
342	0.0544512	0.913103
359	0.0258766	0.70057
368	0.138887	0.574364
379	0.163908	0.448272
394	0.226741	0.305442
407	0.285887	0.271652
429	0.2797	0.189077

Table A.5.: Fit results for the CaA (32 mN/m) system.

T [K]	$A(d^+)$ [a.u.]	$A(r^+)$ [a.u.]
296	0.0193706	1
325	0.00878578	0.962306
342	0.086258	0.863902
359	0.186098	0.671878
368	0.284831	0.503692
379	0.358423	0.34206
394	0.402129	0.233546
407	0.403058	0.183742
429	0.404262	0.131427

A.3. Igor macros

To help with the data processing some automation programs for *WaveMetric Igor Pro* were used:

```
function ProcessLambdaSpectrum()

// ---- PART I ---copy and rename relevant waves

silent 1

Duplicate WLOPG WL
Duplicate SigOsc1 PMT
Duplicate SigOsc2 RefA
Duplicate SigOsc3 RefB
PMT=abs(PMT) // use abs values for PMT wave

//  ---- PART II --- kill zero values from PMT signal wave
Variable k = 0
Variable zc
zc=0
Do
If (PMT[k] == 0)
DeletePoints k,1, WL,PMT,RefA,RefB
zc=zc+1
Else
k = k + 1
Endif
While (k < numpnts(WL))

print "Zero values removed:", zc



// ---- PART III --- make avg values for each wavelength

Variable ActVglParam = 0
Variable ActWL = 0
```

```
Variable AvgPMT = 0
Variable AvgRefA = 0
Variable AvgRefB = 0
Variable PntCounter = 0

Variable j = 0
Variable n = -1
Variable l = 0

Silent 1

Make /N=5000 /D WLa, WNa, PMTa, RefAa, RefBa
Make /N=(numpnts(WL)) /D /O NPnts, WN

Do
If (WL[j] != ActVglParam)
If (n > -1)
WLa[n] = ActWL
PMTa[n] = AvgPMT
RefAa[n] = AvgRefA
RefBa[n] = AvgRefB
NPnts[n] = PntCounter
Endif

ActWL = WL[j]
AvgPMT = 0
AvgRefA = 0
AvgRefB = 0
PntCounter = 0

ActVglParam = WL[j]
n = n + 1
Endif

AvgPMT = AvgPMT*PntCounter/(PntCounter+1) + PMT[j]/(PntCounter+1)
AvgRefA = AvgRefA*PntCounter/(PntCounter+1) + RefA[j]/(PntCounter+1)
```

```
AvgRefB = AvgRefB*PntCounter/(PntCounter+1) + RefB[j]/(PntCounter+1)
PntCounter = PntCounter + 1

j = j + 1

WLa[n] = ActWL
PMTa[n] = AvgPMT
RefAa[n] = AvgRefA
RefBa[n] = AvgRefB

While (j <= numpnts(WL))


l = n + 1

Redimension /N=(l) WLa,WNa
Redimension /N=(l) PMTa, RefAa, RefBa, NPnts

WN=1/WL*1e7
WNa=1/WLa*1e7

// ---- PART IV --- obs.

end

function ProcessFID()

// ---- PART I ---copy and rename relevant waves

silent 1

Duplicate DtLine1 DLPOS
Duplicate SigOsc1 DLPMT
DLPMT=abs(DLPMT) // use abs values for DL PMT wave
```

```
// ---- PART II --- make avg values for each DLPos

Variable ActVglParamDL = 0
Variable ActDLPOS = 0
Variable AvgDLPMT = 0
Variable PntCounterDL = 0

Variable j2 = 0
Variable n2 = -1
Variable l2 = 0

Silent 1

Make /N=5000 /D DLPOSa, DLPMTa
Make /N=(numpnts(DLPos)) /D /O DLNPnts

Do
If (DLPOS[j2] != ActVglParamDL)
If (n2 > -1)
DLPOSa[n2] = ActDLPOS
DLPMTa[n2] = AvgDLPMT
DLNPnts[n2] = PntCounterDL
Endif

ActDLPOS = DLPOS[j2]
AvgDLPMT = 0
PntCounterDL = 0

ActVglParamDL = DLPOS[j2]
n2 = n2 + 1
Endif

AvgDLPMT = AvgDLPMT*PntCounterDL/(PntCounterDL+1) + DLPMT[j2]/(PntCounterDL+1)
PntCounterDL = PntCounterDL + 1

j2 = j2 + 1
```

```
DLPOSa[n2] = ActDLPOS
DLPMTa[n2] = AvgDLPMT

While (j2 <= numpnts(DLPOS))



l2 = n2 + 1

Redimension /N=(l2) DLPOSa
Redimension /N=(l2) DLPMTa, DLNPnts
Killwaves DLNPnts, DLPOS, DLPMT

Display DLPMTa vs DLPOSa
ModifyGraph mode=4,marker=8,lsize=2;DelayUpdate
ModifyGraph tick=2,mirror=1;DelayUpdate
Label left "PMT signal";DelayUpdate
Label bottom "Delay Line 1 Position [ps]"

End
```

A.4. Publications

A.4.1. Refereed papers published

- J. Weber, T. Balgar and E. Hasselbrink
  „Conformational disorder in alkylsiloxane monolayers at elevated temperatures“
  The Journal of Chemical Physics **139**, 244902 (2013); doi: 10.1063/1.4846298

- J. Weber, A. Beier, E. Hasselbrink and T. Balgar
  „Thermally induced conformational changes of Ca-arachidate Langmuir-Blodgett Films at different compression“
  The Journal of Chemical Physics **141**, 044912 (2014); doi: 10.1063/1.4891243

A.4.2. Talks and posters

- Mitarbeiterworkshop 2010, SFB 616
  Papenburg, 17. - 19. May 2010
  „Summenfrequenzspektroskopie an Luft“

- 4th International Workshop on Energy Dissipation at Surfaces
  Kloster Schöntal, 5. - 8. September 2010
  „Vibrational spectroscopy of soft matter interfaces“

- 75. Jahrestagung der DPG und DPG Frühjahrstagung
  Dresden, 13. - 18. March 2011
  „Vibrational spectroscopy of organic monolayers by sum-frequency generation“
  (*Wilhelm und Else Heraeus-Förderprogramm der Deutschen Physikalischen Gesellschaft e. V. zur wissenschaftlichen Kommunikation von Nachwuchsphysikerinnen und -physikern*)

- Mitarbeiterworkshop 2011, SFB 616
  Papenburg, 4. - 6. April 2011
  „Vibrational spectroscopy of interfaces by sum-frequency generation“

- DPG Frühjahrstagung
  Regensburg, 15. March 2013
  „Thermal Influence on the Structure of Alkylsiloxane Monolayers Examined by SFG-Spectroscopy“

(*Wilhelm und Else Heraeus-Förderprogramm der Deutschen Physikalischen Gesellschaft e. V. zur wissenschaftlichen Kommunikation von Nachwuchsphysikerinnen und -physikern*)

- Abschluss Kolloquium 2013, SFB 616
  Bad Honnef, 3. - 8. June 2013
  „Thermal Influence on the Structure of Alkylsiloxane Monolayers examined by SFG-Spectroscopy“

- Neujahrskolloquium der Fakultät für Chemie und des Ortsverbandes Essen-Duisburg der GDCh
  Essen, 8. January 2014
  „Verlust von Ordnung in ultradünnen Schichten“

A.5. Erklärung

Hiermit versichere ich, dass ich die vorliegende Arbeit mit dem Titel

„Temperature induced change in aliphatic monolayers observed by vibrational sum-frequency generation spectroscopy“

selbst verfasst und keine außer den angegebenen Hilfsmitteln und Quellen benutzt habe, und dass die Arbeit in dieser oder ähnlicher Form noch bei keiner anderen Universität eingereicht wurde.

Essen, im August 2014

(J. Weber)

A.6. Danksagung

An dieser Stelle möchte ich mich zunächst herzlich bei meinem Doktorvater, Herrn Prof. Dr. Eckart Hasselbrink, bedanken. Besonders dankbar bin ich für die Aufnahme in eine Arbeitsgruppe, die ich über die Jahre sehr zu schätzen gelernt habe, insbesondere wegen des dort üblichen freundlichen Umgang und Teamgeist. Danke auch für das entgegengebrachte Vertrauen, meine Arbeit eigenverantwortlich und in großer Freiheit durchführen zu dürfen, ohne mich jemals allein gelassen zu fühlen.

Selbstverständlich möchte ich mich auch für die zahlreichen Diskussionen, Anregungen und kritischen Fragen, die zum Gelingen dieser Arbeit und meinem Verständnis von Wissenschaft maßgeblich beigetragen haben, bedanken.

In gleicher Weise gilt mein besonderer Dank Herrn Dr. Thorsten Balgar. Ohne seine wissenschaftliche Anleitung und Hilfestellung in allen Bereichen wäre die Fertigstellung dieser Arbeit nicht möglich gewesen. Vor allem bin ich allerdings dankbar, dass ich in ihm einen Betreuer gefunden habe, mit dem man viel lachen und sich über mehr als nur Wissenschaft unterhalten kann. Nicht zuletzt danke ich dafür, dass er es vor allem war, der mich auch in Zeiten, an denen wenig funktionierte, ermutigt hat, weiter zu machen und das Projekt nicht aufzugeben.

Herzlich bedanken möchte ich mich auch bei Herrn Prof. Dr. Sebastian Schlücker für die Übernahme des Koreferats.

Herrn Prof. Dr. Eckhard Spohr and Herrn Dr. Holger Somnitz danke ich für die Diskussionen zum Thema MD Simulationen.

Dank sei an dieser Stelle auch allen Kolleginnen und Kollegen des Arbeitskreises ausgesprochen für die freundliche Aufnahme in die Gruppe sowie für die Hilfe in verschiedensten Formen. Namentlich sind hier vor allem zu nennen: Elke Normann und Hans Vanheiden für den kurzen Dienstweg zu allen Werkstätten sowie die Unterstützung bei sämtlichen technischen Problemen, Jürgen Leistikow für seinen unermüdlichen Einsatz wider die bockige Elektronik und Sabrina Hilz dafür, die gute Seele des Arbeitskreises zu sein sowie für ihre Hilfe bei allen universitären Formalitäten.

Meinen Bürokollegen, im Besonderen Damian Bürstel, Michael Scheele und Nitha Enasu, danke ich für die gute Arbeitsatmosphäre und Zusammenarbeit sowie dafür,

dass sie es all die Zeit mit meiner lauten Stimme ausgehalten haben.

Andre Beier danke ich für seine Unterstützung bei allen Problemen mit dem Langmuir Trog.

Bedanken möchte ich mich auch bei allen Mitarbeitern des Sonderforschungsbereiches 616 für den wissenschaftlichen und privaten Austausch, im Besonderen auf den gemeinsamen Mitarbeiterworkshops, Summer Schools und Konferenzen.

Mein abschließender Dank gilt meiner Familie und natürlich ganz besonders meinen Eltern, die mir durch ihre vielseitige Unterstützung das Studium erst ermöglicht haben.

Vielen Dank!

A.7. Lebenslauf

Der Lebenslauf ist in der Online-Version aus Gründen des Datenschutzes nicht enthalten.